

---

# Compositional Law Parsing with Latent Random Functions

---

Fan Shi Bin Li\* Xiangyang Xue

Shanghai Key Laboratory of Intelligent Information Processing  
School of Computer Science, Fudan University

fshi22@m.fudan.edu.cn {libin,xyxue}@fudan.edu.cn

## Abstract

Human cognition has compositionality. We understand a scene by decomposing the scene into different concepts (e.g. shape and position of an object) and learning the respective laws of these concepts which may be either natural (e.g. laws of motion) or man-made (e.g. laws of a game). The automatic parsing of these laws indicates the model’s ability to understand the scene, which makes law parsing play a central role in many visual tasks. In this paper, we propose a deep latent variable model for Compositional Law Parsing (CLAP). CLAP achieves the human-like compositionality ability through an encoding-decoding architecture to represent concepts in the scene as latent variables, and further employ concept-specific random functions, instantiated with Neural Processes, in the latent space to capture the law on each concept. Our experimental results demonstrate that CLAP outperforms the compared baseline methods in multiple visual tasks including intuitive physics, abstract visual reasoning, and scene representation. In addition, CLAP can learn concept-specific laws in a scene without supervision and one can edit laws through modifying the corresponding latent random functions, validating its interpretability and manipulability.

## 1 Introduction

Compositionality is an important feature of human cognition [1]. Humans can decompose a scene into individual concepts to learn the respective laws of these concepts, which can be either natural (e.g. laws of motion) or man-made (e.g. laws of a game). When observing a scene of a moving ball, one tends to parse the changing patterns of its appearance and position separately: The appearance stays consistent over time, while the position changes according to the laws of motion. By composing the laws of the ball’s appearance and position, one can understand the changing pattern and predict the status of the moving ball.

Although compositionality has inspired a number of models in visual understanding such as representing handwritten characters through hierarchical decomposition of characters [2, 3] and representing a multi-object scene with object-centric representations [4, 5, 6, 7], automatic parsing of laws in a scene is still a great challenge. For example, to understand the rules in abstract visual reasoning such as Raven’s Progressive Matrices (RPMs) test, the comprehension of attribute-specific representations and the underlying relationships among them is crucial for a model to predict the missing images [8, 9, 10]. To understand the laws of motion in intuitive physics, a model needs to grasp the changing patterns of different attributes (e.g. appearance and position) of each object in a scene to predict the future [11, 12, 13]. However, these methods usually employ neural networks to directly model changing patterns of the scene in a black box, and can hardly abstract the laws of individual concepts in an explicit, interpretable and even manipulable way.

---

\*Corresponding author

A possible solution to enable the abovementioned ability for a model is exploiting a function to represent a law of concept in terms of the representation of the concept itself. To represent a law that may depict arbitrary changing patterns, an expressive and flexible random function is required. The Gaussian Process (GP) is a classical family of random functions that achieves the diversity of function space through different kernel functions [14]. Recently proposed random functions [15, 16, 17, 18, 19, 20, 21, 22, 23] describe function spaces with the powerful nonlinear fitting ability of neural networks. These random functions have been used to capture the changing patterns in a scene, such as mapping timestamps to frames to describe the physical law of moving objects in a video [17, 19, 24]. However, these applications of random functions take images as inputs and the captured laws account for all pixels instead of expected individual concepts.

In this paper, we propose a deep latent variable model for Compositional LAw Parsing (CLAP). CLAP achieves the human-like compositionality ability through an encoding-decoding architecture [25] to represent concepts in the scene as latent variables, and further employ concept-specific random functions in the latent space to capture the law on each concept. By means of the plug-in of different random functions, CLAP gains generality and flexibility applicable to various law parsing tasks. We introduce CLAP-NP as an example that instantiates latent random functions with recently proposed Neural Processes [15].

Our experimental results demonstrate that the proposed CLAP outperforms the compared baseline methods in multiple visual tasks including intuitive physics, abstract visual reasoning, and scene representation. In addition, the experiment on exchanging latent random functions on a specific concept and the experiment on composing latent random functions of the given samples to generate new samples both well demonstrate the *interpretability* and even *manipulability* of the proposed method for compositional law parsing.

## 2 Related Work

Since CLAP focuses on parsing compositional laws which are modeled by latent random functions, compositional scene representation and random functions are highly related to this paper.

**Compositional Scene Representation** Inspired by the compositionality in human cognition, compositional scene representation models understand a scene by object-centric representations. To this end, a class of models initialize object-centric representations first and update them by iterative processes such as Neural Expectation Maximization [26], iterative amortized inference [6], iterative cross-attention [7], and two-stage inference [27]. Another class of models extracts object-centric representations from a scene without iterative inference processes. AIR [4] parses object-centric presence, appearance, and position representations as latent variables. SPACE [28] divides a scene image into small regions and parses region-specific representations in parallel. GNM [29] models the layout of scenes. Recently, many models aim at parsing compositional scene representations in videos [5, 30, 31].

**Random Functions** The GP [14] is a classical family of random functions [14] that regards the outputs of a function as a random variable of multivariate Gaussian distribution. GQN [16] represents 3D scenes as functions by a well-designed representation network and generation network. Conditional Neural Process (CNP) [18] uses a deterministic representation to capture the global structure of functions. To introduce stochasticity in function parsing, NP [15] adopts a Gaussian distributed global random variable  $g$ . ANP [20] overcomes the underfitting problem in NP by combining a deterministic and stochastic computational branch with the attention mechanism. Depending on the way of randomness modeling, context aggregation and output prediction, we can construct different types of function spaces [21, 19, 22, 23]. In addition, some of the few-shot learning methods parse functions from data by learning global variables [32, 33] or adaptive kernels [34, 35]. Another class of methods incorporate latent variable models and ordinary differential equations [36] or stochastic differential equations [37, 38], by which we can describe random functions by the integral over latent states on specific data, e.g., the trajectory of moving balls.

## 3 Preliminaries

A random function is a distribution over function space  $\mathcal{F}$ . By sampling from a random function, we get a function  $f : \mathcal{X} \mapsto \mathcal{Y}$  that maps the input sequence  $\mathbf{x} = (x_1, \dots, x_N)$  to output sequence

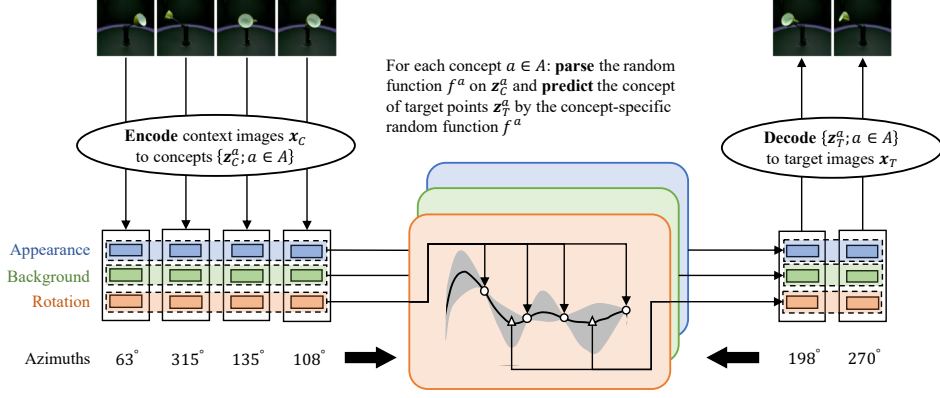


Figure 1: Overview of CLAP: to predict target images, CLAP first encodes given context images into representations of concepts, such as **object appearance**, **background** and **angle of object rotation**; then parses concept-specific latent random functions and computes the representations of concepts in the target images; finally decodes these concepts to compose the target images.

$\mathbf{y} = (\mathbf{y}_1, \dots, \mathbf{y}_N)$ . Suppose that  $D = \{(\mathbf{x}_n, \mathbf{y}_n)\}_{n=1}^N$  is a set of points from  $f \in \mathcal{F}$  that  $\mathbf{y}_n = f(\mathbf{x}_n)$ . By a context index set  $C$  and target index set  $T$ , we divide  $D$  into two subsets  $D_C = \{(\mathbf{x}_c, \mathbf{y}_c) | c \in C\}$  and  $D_T = \{(\mathbf{x}_t, \mathbf{y}_t) | t \in T\}$  where  $D = D_C \cup D_T$  and  $D_C \cap D_T = \emptyset$ . For a random function, an important problem is to find the corresponding function  $f$  according to  $D_C$  and predict target outputs  $\mathbf{y}_t = f(\mathbf{x}_t)$ .

**Neural Process (NP)** The key of the problem is to estimate  $p(\mathbf{y}_T | \mathbf{y}_C, \mathbf{x}_C, \mathbf{x}_T)$ . NP [15] introduces Gaussian distributed global latent variable  $\mathbf{g}$  to represent the stochasticity of functions. In this case, the estimation of  $p(\mathbf{y}_T | \mathbf{y}_C, \mathbf{x}_C, \mathbf{x}_T)$  consists of two steps since  $p(\mathbf{y}_T | \mathbf{y}_C, \mathbf{x}_C, \mathbf{x}_T) = \int \prod_{t \in T} p(\mathbf{y}_t | \mathbf{g}, \mathbf{x}_t) p(\mathbf{g} | \mathbf{y}_C, \mathbf{x}_C) d\mathbf{g}$ . In the first step, an aggregator module extracts the information from context points in  $D_C$  to estimate  $p(\mathbf{g} | \mathbf{y}_C, \mathbf{x}_C) = \mathcal{N}(\mathbf{g} | \boldsymbol{\mu}, \text{diag}(\boldsymbol{\sigma}^2))$  where

$$\boldsymbol{\mu}, \boldsymbol{\sigma} = \mathcal{T}_f \left( \frac{1}{|C|} \sum_{c \in C} \mathcal{T}_a(\mathbf{y}_c, \mathbf{x}_c) \right). \quad (1)$$

In the second step, NP samples the global latent variable  $\mathbf{g}$ , which is combined with  $\mathbf{x}_t$  to independently predict  $\mathbf{y}_t$  by  $p(\mathbf{y}_t | \mathbf{g}, \mathbf{x}_t) = \mathcal{N}(\mathbf{y}_t | \mathcal{T}_p(\mathbf{g}, \mathbf{x}_t), \sigma^2 \mathbf{I})$ . Neural networks  $\mathcal{T}_a$ ,  $\mathcal{T}_f$  and  $\mathcal{T}_p$  increase the model capacity of NP to learn data-specific function spaces.

**Generative Query Network (GQN)** GQN [16] has a similar computational process as NP, but it focuses on the scene representation. GQN regards mappings from the camera pose in 3D scenes to the corresponding image as a random function, where a deterministic neural scene representation  $\mathbf{r} = \sum_{c \in C} \mathcal{T}_a(\mathbf{y}_c, \mathbf{x}_c)$  and a latent variable  $\mathbf{z}$  capture the information and stochasticity of scene. By means of well-designed representation network  $\mathcal{T}_a$  and generation network  $\mathcal{T}_p$ , GQN succeed to generate target scene images  $\mathbf{y}_t \sim \mathcal{N}(\mathbf{y}_t | \mathcal{T}_p(\mathbf{r}, \mathbf{z}, \mathbf{x}_t), \sigma^2 \mathbf{I})$  from given context scene images.

## 4 Model

Figure 1 is an overview of CLAP. First, an encoder converts context images to individual concepts in the latent space. Then CLAP parses concept-specific random functions on the context visual concepts, which are exploited to predict the target concepts. Finally, a decoder maps the target concepts to target images. The concept-specific latent random functions achieve the compositional law parsing in CLAP. In the following part, we will introduce the generative process, variational inference, and parameter learning of CLAP. At the end of this section, we propose CLAP-NP, an instance that instantiates the latent random function with NP.

### 4.1 Latent Random Functions

Given  $D_C$  and  $D_T$ , the objective of CLAP is to maximize log-likelihood  $\log p(\mathbf{y}_T | \mathbf{y}_C, \mathbf{x})$ . In the framework of conditional latent variable models, we introduce a variational posterior  $q(\mathbf{h} | \mathbf{y}, \mathbf{x})$  for

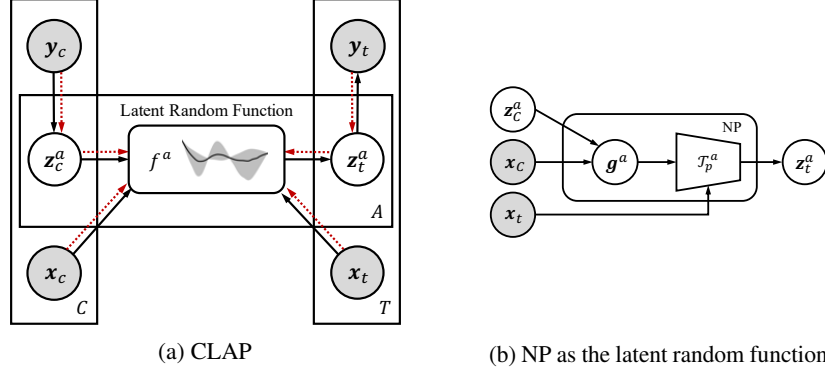


Figure 2: The graphical model of CLAP where the generative process is indicated by black solid lines and the variational inference is indicated by red dotted lines. Panel (a) shows the framework of CLAP, where the latent random function  $f^a$  for the concept  $a \in A$  can be instantiated by arbitrary random functions; Panel (b) describes how to instantiate the latent random function with NP.

the latent variable  $\mathbf{h}$ , and approximate log-likelihood by evidence lower bound (ELBO) [39]:

$$\log p(\mathbf{y}_T | \mathbf{y}_C, \mathbf{x}) \geq \mathbb{E}_{q(\mathbf{h} | \mathbf{y}, \mathbf{x})} [\log p(\mathbf{y}_T | \mathbf{h})] - \mathbb{E}_{q(\mathbf{h} | \mathbf{y}, \mathbf{x})} \left[ \log \frac{q(\mathbf{h} | \mathbf{y}, \mathbf{x})}{p(\mathbf{h} | \mathbf{y}_C, \mathbf{x})} \right] = \mathcal{L}. \quad (2)$$

The detailed derivation is shown in Supplementary Materials. The latent variable  $\mathbf{h}$  includes the local information of images  $\mathbf{z} = \{\mathbf{z}_n\}_{n=1}^N$  where  $\mathbf{z}_n$  is the low-dimensional representation of  $\mathbf{x}_n$ . Moreover, we decompose  $\mathbf{z}_n$  into independent concepts  $\{\mathbf{z}_n^a | a \in A\}$  (e.g., an image of a single-object scene may have concepts such as object appearance, illumination, camera orientation, etc.) where  $A$  refers to the name set of these concepts. Assuming that these concepts satisfy their respective change patterns, we employ independent latent random functions to capture the law of each concept. Denote the latent random function on the concept  $a$  as  $f^a$ , the specific form of  $f^a$  depends on the way we model it. As Figure 2b shows, if adopting NP as the latent random function, we have  $f^a(\mathbf{x}_t) = \mathcal{T}_p^a(\mathbf{g}^a, \mathbf{x}_t)$  where  $\mathbf{g}^a$  is a Gaussian-distributed latent variable to control the randomness of  $f^a$ . Within the graphical model of CLAP in Figure 2a, the prior and posterior in  $\mathcal{L}$  are factorized into

$$\begin{aligned} p(\mathbf{h} | \mathbf{y}_C, \mathbf{x}) &= \prod_{a \in A} \left( p(f^a | \mathbf{z}_C^a, \mathbf{x}_C) \prod_{t \in T} p(\mathbf{z}_t^a | f^a, \mathbf{z}_C^a, \mathbf{x}_C, \mathbf{x}_t) \prod_{c \in C} p(\mathbf{z}_c^a | \mathbf{y}_c) \right) \\ p(\mathbf{y}_T | \mathbf{h}) &= \prod_{t \in T} p(\mathbf{y}_t | \mathbf{z}_t), \quad q(\mathbf{h} | \mathbf{y}, \mathbf{x}) = \prod_{a \in A} \left( q(f^a | \mathbf{z}^a, \mathbf{x}) \prod_{c \in C} q(\mathbf{z}_c^a | \mathbf{y}_c) \prod_{t \in T} q(\mathbf{z}_t^a | \mathbf{y}_t) \right) \end{aligned} \quad (3)$$

Decomposing  $f$  into concept-specific laws  $\{f^a | a \in A\}$  in the above process is critical for CLAP's compositionality. The compositionality makes it possible to parse only several concept-specific laws rather than the entire law on  $\mathbf{z}$ , which reduces the complexity of law parsing while increasing the interpretability of laws. The interpretability allows us to edit laws, for example, exchanging the law on some concepts and composing the laws of existing samples.

## 4.2 Parameter Learning

Based on the detailed priors and posteriors in Equation 3, we factorize ELBO as (See Supplementary Materials for the detailed derivation)

$$\begin{aligned} \mathcal{L} &= \underbrace{\sum_{t \in T} \mathbb{E}_{q(\mathbf{h} | \mathbf{y}, \mathbf{x})} [\log p(\mathbf{y}_t | \mathbf{z}_t)]}_{\text{Reconstruction term } \mathcal{L}_r} - \underbrace{\sum_{a \in A} \sum_{t \in T} \mathbb{E}_{q(\mathbf{h} | \mathbf{y}, \mathbf{x})} \left[ \log \frac{q(\mathbf{z}_t^a | \mathbf{y}_t)}{p(\mathbf{z}_t^a | f^a, \mathbf{z}_C^a, \mathbf{x}_C, \mathbf{x}_t)} \right]}_{\text{Target regularizer } \mathcal{L}_t} \\ &\quad - \underbrace{\sum_{a \in A} \mathbb{E}_{q(\mathbf{h} | \mathbf{y}, \mathbf{x})} \left[ \log \frac{q(f^a | \mathbf{z}^a, \mathbf{x})}{p(f^a | \mathbf{z}_C^a, \mathbf{x}_C)} \right]}_{\text{Function regularizer } \mathcal{L}_f} - \underbrace{\sum_{a \in A} \sum_{c \in C} \mathbb{E}_{q(\mathbf{h} | \mathbf{y}, \mathbf{x})} \left[ \log \frac{q(\mathbf{z}_c^a | \mathbf{y}_c)}{p(\mathbf{z}_c^a | \mathbf{y}_c)} \right]}_{\text{Context regularizer } \mathcal{L}_c} \end{aligned} \quad (4)$$

**Reconstruction Term**  $\mathcal{L}_r$  is the sum of the log-likelihood  $\log p(\mathbf{y}_t|\mathbf{z}_t)$  of each target image.  $p(\mathbf{y}_t|\mathbf{z}_t)$  is modelled by a decoder that converts concepts to the distribution parameter of target images. CLAP maximizes  $\mathcal{L}_r$  to connect the latent space with the image space, enabling the decoder to generate high-quality images.

**Target Regularizer**  $\mathcal{L}_t$  consists of Kullback–Leibler (KL) divergences between the posterior  $q(\mathbf{z}_t^a|\mathbf{y}_t)$  and the prior  $p(\mathbf{z}_t^a|f^a, \mathbf{z}_C^a, \mathbf{x}_C, \mathbf{x}_t)$  of target concepts. In  $q(\mathbf{z}_t^a|\mathbf{y}_t)$ , the distribution of target concepts is computed directly from the target image by the encoder, so it usually contains more accurate information. And in  $p(\mathbf{z}_t^a|f^a, \mathbf{z}_C^a, \mathbf{x}_C, \mathbf{x}_t)$ , the distribution of the target concept is estimated from the context. The minimization of  $\mathcal{L}_t$  fills the gap between the posterior and prior and ensures the accuracy of predictors.

**Function Regularizer**  $\mathcal{L}_f$  consists of KL divergences between the posterior  $q(f^a|\mathbf{z}^a, \mathbf{x})$  and the prior  $p(f^a|\mathbf{z}_C^a, \mathbf{x}_C)$ . We use  $\mathcal{L}_f$  as a measure of function consistency to ensure that model can obtain similar distributions for  $f^a$  with any subset  $\mathbf{z}_C^a \subseteq \mathbf{z}^a$  and  $\mathbf{x}_C \subseteq \mathbf{x}$  as inputs. To this end, CLAP shares concept-specific function parsers to model  $q(f^a|\mathbf{z}^a, \mathbf{x})$  and  $p(f^a|\mathbf{z}_C^a, \mathbf{x}_C)$ . And we need to design the architecture of function parsers so that it can take different subsets as input.

**Context Regularizer**  $\mathcal{L}_c$  consists of KL divergences between the posterior  $q(\mathbf{z}_c^a|\mathbf{y}_c)$  and the prior  $p(\mathbf{z}_c^a|\mathbf{y}_c)$  of context concepts. To avoid mismatch between the posterior and prior and cut down model parameters, the posterior and prior are parameterized with the same encoder. In this case, we have  $p(\mathbf{z}_c^a|\mathbf{y}_c) = q(\mathbf{z}_c^a|\mathbf{y}_c)$  and further  $\mathcal{L}_c = 0$ . So we remove  $\mathcal{L}_c$  from Equation 4.

Correct decomposition of concepts are essential for model performance. However, CLAP is trained without additional supervision to guide the learning of concepts. Although CLAP explicitly defines independent concepts in priors and posteriors, it is not sufficient to automatically decompose concepts for some complex data. To solve the problem, CLAP can introduce extra inductive biases: design encoder and decoder to artificially decompose concepts, e.g., spatial transformation layers helps to decompose spatial and non-spatial concepts [40]; or we can modify ELBO, e.g.,  $\beta$ -VAE utilizes hyperparameters to control regularizers [41], and  $\beta$ -TCVAE adds a total correlation (TC) regularizer  $\mathcal{R}_{TC}$  to help disentanglement [42]. Here we choose to modify ELBO of CLAP, and finally the optimization objective is

$$\operatorname{argmax}_{p,q} \mathcal{L}^* = \operatorname{argmax}_{p,q} \mathcal{L}_r - \beta_t \mathcal{L}_t - \beta_f \mathcal{L}_f - \beta_{TC} \mathcal{R}_{TC} \quad (5)$$

where  $\beta_t, \beta_f, \beta_{TC}$  are hyperparameters that regulate the importance of regularizers in the training process. We can compute  $\mathcal{L}^*$  by Stochastic Gradient Variational Bayes (SGVB) estimator [43] and update parameters by gradient descent optimizers [44].

### 4.3 NP as Latent Random Function

In this subsection, we propose CLAP-NP as an example that instantiates the latent random function with NP. According to NP, we employ a latent variable  $\mathbf{g}^a$  to control the randomness of the latent random function  $f^a$  for each concept in CLAP-NP.

**Generative Process** CLAP-NP first encodes each context image  $\mathbf{x}_c$  to concepts:

$$\begin{aligned} \{\mu_{z,c}^a | a \in A\} &= \text{Encoder}(\mathbf{x}_c), & c \in C, \\ \mathbf{z}_c^a &\sim \mathcal{N}(\mu_{z,c}^a, \sigma_z^2 \mathbf{I}), & a \in A, c \in C. \end{aligned} \quad (6)$$

To stabilize the learning of concepts, the encoder outputs only the mean of Gaussian distribution, with the standard deviation as a hyperparameter. Using the process in Equation 1 for each concept, a concept-specific function parser aggregates the contextual information and transform it to the mean  $\mu_g^a$  and standard deviation  $\sigma_g^a$  of  $\mathbf{g}^a$ . The concept-specific target predictor takes  $\mathbf{g}^a \sim \mathcal{N}(\mu_g^a, \text{diag}(\sigma_g^2))$  and  $\mathbf{x}_t$  as inputs and output the mean  $\mu_{z,t}^a$  of  $\mathbf{z}_t$ , leaving the standard deviation as a hyperparameter. To keep independence between concepts, CLAP-NP introduces identical but independent function parsers and target predictors. Once all of the concepts  $\mathbf{z}_t^a \sim \mathcal{N}(\mu_{z,t}^a, \sigma_z^2 \mathbf{I})$  for  $a \in A$  are generated, we concatenate and decode them into target images:

$$\mathbf{x}_t \sim \mathcal{N}(\mu_{x,t}, \sigma_x^2 \mathbf{I}), \quad \mu_{x,t} = \text{Decoder}(\{\mathbf{z}_t^a | a \in A\}), \quad t \in T. \quad (7)$$

Table 1: MSEs on BoBa, CRPM, and MPI3D dataset

Model	BoBa-1		BoBa-2	
	MSE-2	MSE-4	MSE-2	MSE-4
NP	0.4696 $\pm$ 0.0159	0.9637 $\pm$ 0.0419	0.9892 $\pm$ 0.0440	2.0948 $\pm$ 0.1237
GQN	0.4917 $\pm$ 0.0574	3.2788 $\pm$ 0.2540	1.3388 $\pm$ 0.2495	6.1097 $\pm$ 0.2686
CLAP-NP	<b>0.0519 <math>\pm</math> 0.0022</b>	<b>0.1137 <math>\pm</math> 0.0080</b>	<b>0.5689 <math>\pm</math> 0.0876</b>	<b>1.5806 <math>\pm</math> 0.4129</b>
Model	CRPM-double-triangle		CRPM-double-circle	
	MSE-2	MSE-3	MSE-2	MSE-3
NP	0.1651 $\pm$ 0.0219	0.2912 $\pm$ 0.0201	0.5160 $\pm$ 0.0339	0.8093 $\pm$ 0.0437
GQN	0.7207 $\pm$ 0.0577	1.5119 $\pm$ 0.0744	1.6844 $\pm$ 0.0646	3.2832 $\pm$ 0.0938
CLAP-NP	<b>0.0386 <math>\pm</math> 0.0022</b>	<b>0.0814 <math>\pm</math> 0.0521</b>	<b>0.1982 <math>\pm</math> 0.0882</b>	<b>0.5053 <math>\pm</math> 0.1875</b>
Model	MPI3D			
	MSE-2	MSE-5	MSE-10	MSE-20
NP	0.2523 $\pm$ 0.0183	0.7067 $\pm$ 0.0316	4.4087 $\pm$ 0.0582	9.0118 $\pm$ 0.0787
GQN	<b>0.0240 <math>\pm</math> 0.0007</b>	0.5809 $\pm$ 0.0100	11.8556 $\pm$ 0.0688	17.6639 $\pm$ 0.0528
CLAP-NP	0.0950 $\pm$ 0.0045	<b>0.3441 <math>\pm</math> 0.0269</b>	<b>1.6057 <math>\pm</math> 0.0081</b>	<b>3.2524 <math>\pm</math> 0.0138</b>

To control the noise in sampled images, we introduce a hyperparameter  $\sigma_x$  as the standard deviation. As Figure 2 shows, we can rewrite the prior  $p(\mathbf{h}|\mathbf{y}_C, \mathbf{x})$  in CLAP-NP as

$$p(\mathbf{h}|\mathbf{y}_C, \mathbf{x}) = \prod_{a \in A} \left( p(\mathbf{g}^a | \mathbf{z}_C^a, \mathbf{x}_C) \prod_{t \in T} p(\mathbf{z}_t^a | \mathbf{g}^a, \mathbf{x}_t) \prod_{c \in C} p(\mathbf{z}_c^a | \mathbf{y}_c) \right). \quad (8)$$

**Inference and Learning** In the variational inference, other than that the randomness of  $f^a$  is replaced by  $\mathbf{g}^a$ , the posterior of CLAP-NP is the same as that in Equation 3:

$$q(\mathbf{h}|\mathbf{y}, \mathbf{x}) = \prod_{a \in A} \left( q(\mathbf{g}^a | \mathbf{z}^a, \mathbf{x}) \prod_{c \in C} q(\mathbf{z}_c^a | \mathbf{y}_c) \prod_{t \in T} q(\mathbf{z}_t^a | \mathbf{y}_t) \right). \quad (9)$$

In the first stage, we compute the mean of both  $\mathbf{z}_C$  and  $\mathbf{z}_T$  by the encoder. Because CLAP shares the encoder in the prior and posterior, in the training process we can use the results in Equation 6 of the generative process instead of recalculating the mean of  $\mathbf{z}_C$ . Then we compute the distribution parameters of  $\mathbf{g}^a$  by the shared concept-specific function parsers in generative process where the input in the variational inference are  $\mathbf{z}^a$  and  $\mathbf{x}$  instead of  $\mathbf{z}_C^a$  and  $\mathbf{x}_C$ . With the above  $p(\mathbf{h}|\mathbf{y}_C, \mathbf{x})$  and  $q(\mathbf{h}|\mathbf{y}, \mathbf{x})$ , ELBO of CLAP-NP is

$$\mathcal{L}_t = \sum_{a \in A} \sum_{t \in T} \mathbb{E}_{q(\mathbf{h}|\mathbf{y}, \mathbf{x})} \left[ \log \frac{q(\mathbf{z}_t^a | \mathbf{y}_t)}{p(\mathbf{z}_t^a | \mathbf{g}^a, \mathbf{x}_t)} \right], \quad \mathcal{L}_f = \sum_{a \in A} \mathbb{E}_{q(\mathbf{h}|\mathbf{y}, \mathbf{x})} \left[ \log \frac{q(\mathbf{g}^a | \mathbf{z}^a, \mathbf{x})}{p(\mathbf{g}^a | \mathbf{z}_C^a, \mathbf{x}_C)} \right]. \quad (10)$$

The other subterms are not listed here because they are the same as in Equation 4.

## 5 Experiments

To evaluate the model’s ability to parse the laws of individual concepts on different types of data, we use three datasets in the experiments: (1) **bouncing ball** (abbreviated as **BoBa**) dataset [31] to validate the ability of intuitive physics; (2) **Continuous Raven’s Progressive Matrix (CRPM)** dataset [45] to validate the ability of abstract visual reasoning; (3) **MPI3D** dataset [46] to validate the ability of scene representation. Although there have been methods that can solve the tasks such as intuitive physics by latent random functions [32, 38], they do not decompose physical laws into concept-specific latent random functions and thus lack interpretability and manipulability.

In quantitative experiments, Mean Squared Errors (MSEs) between predictions and ground truths are used as the evaluation metric. Because of the randomness of splitting data and sampling random variables, we perform the evaluation procedure 10 times and take the average of MSEs as the result.

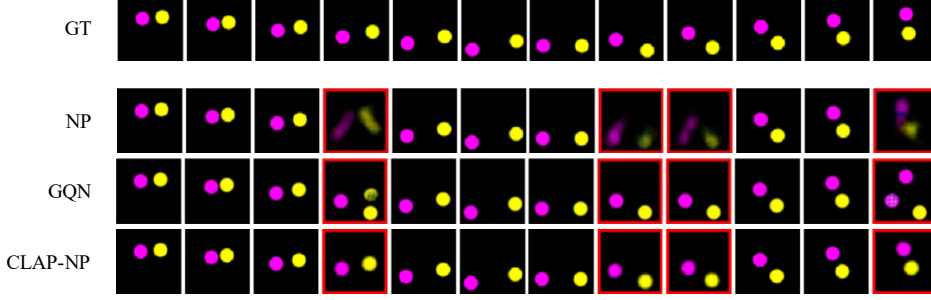


Figure 3: Prediction results on BoBa-2 dataset where the red box indicates the target images and the black box indicates the context images.

To evaluate models from easy to difficult, we apply different amounts of target images to each dataset. More detailed descriptions and experimental results can be found in Supplementary Materials.

**Compared baselines** We use NP [15] and GQN [16] as compared baselines. Because CLAP-NP instantiates the latent random function with NP, we include NP as one of the baselines. Although there are similar processes to model the randomness of functions in NP and CLAP-NP, they have significant differences: NP models the changing patterns of images directly; while CLAP-NP models the changing patterns of concepts in the latent space. GQN is selected as a baseline since it models the distribution of image-valued functions, which highly fits our experimental settings. Considering that NP is not used to model image-valued functions, we need to add an additional encoder and decoder to NP’s aggregator and predictor to help it handle high-dimensional images.

### 5.1 Intuitive Physics

Intuitive physics is the underlying knowledge for humans to understand and predict the evolution of the physical world [12]. We use BoBa dataset with colored bouncing balls to evaluate the model’s intuitive physics of object collisions. BoBa-1 and BoBa-2 are respectively one-ball and two-ball instances of BoBa. In BoBa, we represent the physical law of collisions as functions mapping timestamps  $x \in \mathbb{R}$  to video frames  $y \in \mathbb{R}^{3HW}$ . In the prediction of target video frames, models need to learn the consistency law of appearance and the collision law of position. As Table 1 shows, it is more challenging to understand laws on BoBa-2 since the model needs to learn not only the collision between balls and borders but the more complicated collision between balls.

In the experiment, MSE-2 and MSE-4 indicate that we select 2 and 4 video frames as target images. Table 1 illustrates CLAP-NP’s intuitive physics because it achieves the best MSE-2 and MSE-4 scores on both BaBo-1 and BaBo-2. Figure 3 shows the prediction results where NP generates blurred images. GQN has the potential to generate non-existent balls, which evidences that it is difficult for GQN to understand the consistency of the number of balls in the scene. Due to the compositionality, CLAP-NP captures the color consistency and physical laws (mainly the laws of collision, i.e., how the velocity changes before and after collisions) of the moving balls.

### 5.2 Abstract Visual Reasoning

Abstract visual reasoning is a manifestation of human’s fluid intelligence [47, 47]. RPM [48] is a famous nonverbal test widely used to estimate the model’s abstract visual reasoning ability. RPM is a  $3 \times 3$  image matrix, and the changing rule of the entire matrix consists of the subrule (e.g., progressive change or constant change) on attributes. In this experiment, we adopt CRPM to test models to predict the missing images of the matrix.

In this experiment, MSE-2 and MSE-3 indicate that we randomly remove 2 and 3 images from the problem panel as target images. Table 1 shows that our model achieves the best results in both the MSE-2 and MSE-3. Figure 4 displays the predictions on CRPM-double-circle and CRPM-double-triangle where NP struggles to generate high-quality predictions and tends to produce ambiguous areas. GQN generates the same image at all missing positions and fails to plot sectors on CRPM-double-circle. The predictions of the compared baselines indicate that they lack an understanding of concept-specific rules.

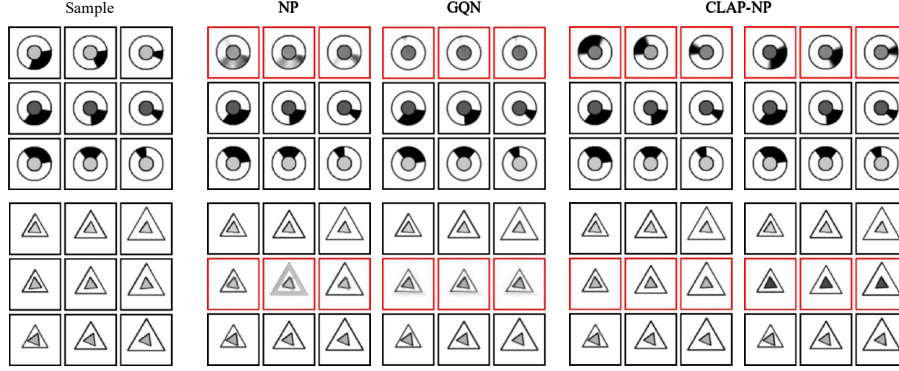


Figure 4: Prediction results on CRPM-double-circle dataset.

Figure 4 displays the different predictions of the same context for CLAP-NP. It is worth stressing that the answer to a CRPM is not unique when we remove the entire line of images from it. In the first sample of Figure 4, all the predictions with progressive changes in the sector size are correct. The prediction results indicate that CLAP-NP learns progressive (increases or decreases by a fixed step in the row) and constant laws (keeps invariant in the row) on attributes, rather than simple context-to-target mappings.

### 5.3 Scene Representation

In scene representation, we use MPI3D dataset where each scene contains a circular platform with colored edges. A robotic arm in the center of the platform is attached to the bottom of a 3D object with different shapes (such as bowls, cups, etc.), colors, and sizes. The robotic arm can manipulate the altitude and azimuth of the object, and the camera has three different heights. By representing the law of scene images as a random function, inputs  $x \in \mathbb{R}$  are altitudes or azimuths of the object and outputs  $y \in \mathbb{R}^{3HW}$  are RGB images corresponding to the input. To predict correct target images, models need to observe context images and understand the changing pattern of the scene.

In the training phase, we provide 8 images for each scene and randomly select 1 to 4 of them as target images. In the test phase, we use two configurations. In the first configuration, we provide 8 images and select 2 or 5 of them as target images (MSE-2 and MSE-5). In the second configuration, we provide 40 scene images, 10 or 20 of which are target images (MSE-10 and MSE-20). The laws learned here are rotations of centric objects along altitude or azimuth. Table 1 shows that in both configurations our model outperforms NP. And compared with GQN, our model has lower MSE-2 but higher MSE-5, MSE-10, and MSE-20. Since GQN aims at scene representation, its network architecture has good inductive biases when the test configuration is close to the training one (MSE-2). However, the decrease in the MSE-5, MSE-10, and MSE-20 indicates that GQN can hardly generalize the learned laws to novel situations with more images. Compositionality allows CLAP-NP to model only concept-specific subrules. In this case, it is more convenient for models to obtain a representation of function with generalizability.

### 5.4 Compositionality of Laws

The compositionality of CLAP makes it possible to edit laws of specific concepts, such as exchanging latent random functions between samples and generating samples with new laws by composing latent random functions of existing samples. The direct edits to concept-specific latent random functions reflect the interpretability and manipulability of our model.

**Latent Random Function Exchange** The compositionality allows us to swap the law of the particular concept between samples: we first use the inference process to obtain the global latent variables  $g_1$  and  $g_2$  for two samples; then swap the latent variables  $g_1^a$  and  $g_2^a$  corresponding to the concept  $a$ ; finally the generative process regenerate two videos with the concept  $a$  swapped. As shown in Figure 5, in the first example, we exchange the color of the balls; and in the second example, we exchange the altitude and azimuth of the object. For the first example, the time-invariant color is successfully swapped, which evidences that our model can automatically learn the constant laws



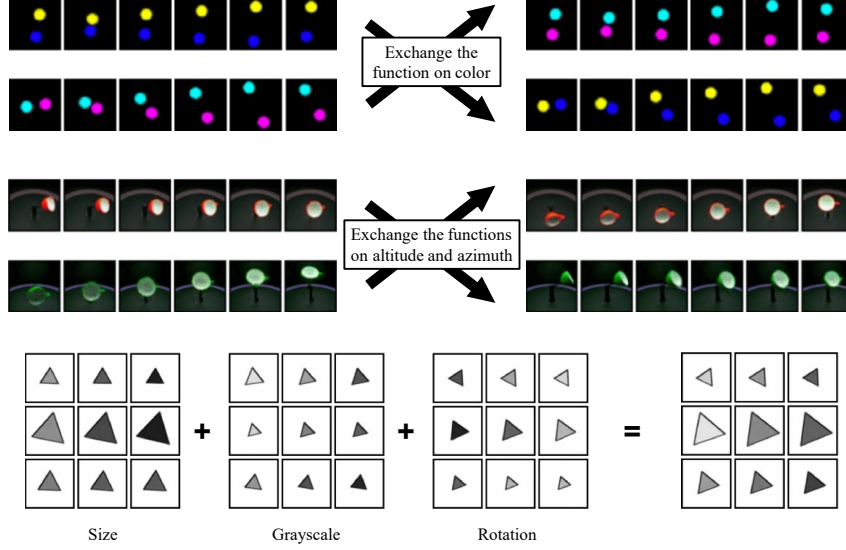


Figure 5: Edit latent random functions. Exchange latent random functions (top two rows): modify the specific concept of samples by swapping their latent random functions on BoBa-2 and MPI3D dataset. Compose latent random functions (bottom): generate a novel sample by composing the latent random functions on size, grayscale and rotation from three different samples on CRPM-triangle dataset.

and collision laws from the video. For the second example, we also show that the swapping of latent random functions can be performed on two concepts at the same time.

**Latent Random Function Composition** In this experiment, we generate a sample with new laws by combining the latent random function from existing samples. As shown in Figure 5, we first infer the global latent variables  $\{(g_k^s, g_k^g, g_k^r)\}_{k=1}^3$  of size, grayscale, and rotation for three given samples; then select  $g_1^s$ ,  $g_2^g$ , and  $g_3^r$  from three samples respectively, which are combined and decoded to generate the sample with new laws. It is worth stating that the composition process described above is close to the way a human designs RPMs, which indicates that our model achieves the compositionality of laws. In addition, the composition of latent random functions provides a way for us to generate new samples based on existing samples [3].

## 6 Conclusion and Limitation

Inspired by the compositionality in human cognition, we propose a deep latent variable model for Compositional Law Parsing (CLAP). CLAP decomposes high-dimensional images into independent visual concepts in the latent space and employs latent random functions to capture the concept-changing laws, by which CLAP achieves the compositionality of laws. To instantiate CLAP, we propose CLAP-NP that uses NPs as latent random functions. The experimental results demonstrate the benefits of our model in intuitive physics, abstract visual reasoning, and scene representation. Through the experiments on latent random function exchange and composition, we further qualitatively evaluate the interpretability and manipulability of the learned functions in CLAP.

We conclude our limitations in three aspects. (1) **Complexity and variety of datasets.** We have evaluated CLAP’s compositional law parsing ability on three datasets with different types of relatively simple and clear laws. Parsing compositional laws in more complex situations (e.g., real-world scenes, complex laws) will be explored in future works. (2) **Evaluation of law compositionality.** MSEs in experiments can hardly measure the compositionality of learned laws. In future works, we can borrow the idea of disentanglement metrics and set up new metrics to evaluate the compositionality of the learned laws. (3) **Concept decomposition.** Concept decomposition is critical for achieving the compositionality of laws in CLAP. In order to apply CLAP to more complicated data in future works, it is necessary to discover more powerful concept decomposition methods (to replace the  $\beta$ -VAE or  $\beta$ -TCVAE regularization adopted in CLAP) or, if needed, work with additional supervised information to learn concepts.

## References

- [1] Lake, B. M., T. D. Ullman, J. B. Tenenbaum, et al. Building machines that learn and think like people. *Behavioral and brain sciences*, 40, 2017.
- [2] Lake, B., R. Salakhutdinov, J. Gross, et al. One shot learning of simple visual concepts. In *Proceedings of the annual meeting of the cognitive science society*, vol. 33. 2011.
- [3] Lake, B. M., R. Salakhutdinov, J. B. Tenenbaum. Human-level concept learning through probabilistic program induction. *Science*, 350(6266):1332–1338, 2015.
- [4] Eslami, S., N. Heess, T. Weber, et al. Attend, infer, repeat: Fast scene understanding with generative models. *Advances in Neural Information Processing Systems*, 29, 2016.
- [5] Kosioerek, A., H. Kim, Y. W. Teh, et al. Sequential attend, infer, repeat: Generative modelling of moving objects. *Advances in Neural Information Processing Systems*, 31, 2018.
- [6] Greff, K., R. L. Kaufman, R. Kbra, et al. Multi-object representation learning with iterative variational inference. In *International Conference on Machine Learning*, pages 2424–2433. PMLR, 2019.
- [7] Locatello, F., D. Weissenborn, T. Unterthiner, et al. Object-centric learning with slot attention. *Advances in Neural Information Processing Systems*, 33:11525–11538, 2020.
- [8] Santoro, A., F. Hill, D. Barrett, et al. Measuring abstract reasoning in neural networks. In *International Conference on Machine Learning*, pages 4477–4486. 2018.
- [9] Steenbrugge, X., S. Leroux, T. Verbelen, et al. Improving generalization for abstract reasoning tasks using disentangled feature representations. *arXiv preprint arXiv:1811.04784*, 2018.
- [10] Wu, Y., H. Dong, R. Grosse, et al. The scattering compositional learner: Discovering objects, attributes, relationships in analogical reasoning. *arXiv preprint arXiv:2007.04212*, 2020.
- [11] Agrawal, P., A. V. Nair, P. Abbeel, et al. Learning to poke by poking: Experiential learning of intuitive physics. *Advances in neural information processing systems*, 29, 2016.
- [12] Kubricht, J. R., K. J. Holyoak, H. Lu. Intuitive physics: Current research and controversies. *Trends in cognitive sciences*, 21(10):749–759, 2017.
- [13] Ye, T., X. Wang, J. Davidson, et al. Interpretable intuitive physics model. In *Proceedings of the European Conference on Computer Vision (ECCV)*, pages 87–102. 2018.
- [14] Williams, C. K., C. E. Rasmussen. *Gaussian processes for machine learning*, vol. 2. MIT press Cambridge, MA, 2006.
- [15] Garnelo, M., J. Schwarz, D. Rosenbaum, et al. Neural processes. *arXiv preprint arXiv:1807.01622*, 2018.
- [16] Eslami, S. A., D. Jimenez Rezende, F. Besse, et al. Neural scene representation and rendering. *Science*, 360(6394):1204–1210, 2018.
- [17] Kumar, A., S. Eslami, D. J. Rezende, et al. Consistent generative query networks. *arXiv preprint arXiv:1807.02033*, 2018.
- [18] Garnelo, M., D. Rosenbaum, C. Maddison, et al. Conditional neural processes. In *International Conference on Machine Learning*, pages 1704–1713. PMLR, 2018.
- [19] Singh, G., J. Yoon, Y. Son, et al. Sequential neural processes. *Advances in Neural Information Processing Systems*, 32, 2019.
- [20] Kim, H., A. Mnih, J. Schwarz, et al. Attentive neural processes. In *International Conference on Learning Representations*. 2019.
- [21] Louizos, C., X. Shi, K. Schutte, et al. The functional neural process. *Advances in Neural Information Processing Systems*, 32, 2019.
- [22] Lee, J., Y. Lee, J. Kim, et al. Bootstrapping neural processes. *Advances in neural information processing systems*, 33:6606–6615, 2020.
- [23] Foong, A., W. Bruinsma, J. Gordon, et al. Meta-learning stationary stochastic process prediction with convolutional neural processes. *Advances in Neural Information Processing Systems*, 33:8284–8295, 2020.

- [24] Fortuin, V., D. Baranchuk, G. Rätsch, et al. Gp-vae: Deep probabilistic time series imputation. In *International conference on artificial intelligence and statistics*, pages 1651–1661. PMLR, 2020.
- [25] Hamrick, J. B., K. R. Allen, V. Bapst, et al. Relational inductive bias for physical construction in humans and machines. *arXiv preprint arXiv:1806.01203*, 2018.
- [26] Greff, K., S. Van Steenkiste, J. Schmidhuber. Neural expectation maximization. *Advances in Neural Information Processing Systems*, 30, 2017.
- [27] Emami, P., P. He, S. Ranka, et al. Efficient iterative amortized inference for learning symmetric and disentangled multi-object representations. In *International Conference on Machine Learning*, pages 2970–2981. PMLR, 2021.
- [28] Lin, Z., Y.-F. Wu, S. V. Peri, et al. Space: Unsupervised object-oriented scene representation via spatial attention and decomposition. *arXiv preprint arXiv:2001.02407*, 2020.
- [29] Jiang, J., S. Ahn. Generative neurosymbolic machines. *Advances in Neural Information Processing Systems*, 33:12572–12582, 2020.
- [30] Jiang, J., S. Janghorbani, G. De Melo, et al. Scalor: Generative world models with scalable object representations. *arXiv preprint arXiv:1910.02384*, 2019.
- [31] Lin, Z., Y.-F. Wu, S. Peri, et al. Improving generative imagination in object-centric world models. In *International Conference on Machine Learning*, pages 6140–6149. PMLR, 2020.
- [32] Wu, T., J. Peurifoy, I. L. Chuang, et al. Meta-learning autoencoders for few-shot prediction. *arXiv preprint arXiv:1807.09912*, 2018.
- [33] Gordon, J., J. Bronskill, M. Bauer, et al. Meta-learning probabilistic inference for prediction. In *International Conference on Learning Representations*. 2019.
- [34] Tossou, P., B. Dura, F. Laviolette, et al. Adaptive deep kernel learning. *arXiv preprint arXiv:1905.12131*, 2019.
- [35] Patacchiola, M., J. Turner, E. J. Crowley, et al. Bayesian meta-learning for the few-shot setting via deep kernels. *Advances in Neural Information Processing Systems*, 33:16108–16118, 2020.
- [36] Norcliffe, A., C. Bodnar, B. Day, et al. Neural ode processes. In *International Conference on Learning Representations*. 2021.
- [37] Li, X., T.-K. L. Wong, R. T. Chen, et al. Scalable gradients for stochastic differential equations. In *International Conference on Artificial Intelligence and Statistics*, pages 3870–3882. PMLR, 2020.
- [38] Hasan, A., J. M. Pereira, S. Farsiu, et al. Identifying latent stochastic differential equations. *IEEE Transactions on Signal Processing*, 70:89–104, 2021.
- [39] Sohn, K., H. Lee, X. Yan. Learning structured output representation using deep conditional generative models. *Advances in neural information processing systems*, 28:3483–3491, 2015.
- [40] Skafté, N., S. Hauberg. Explicit disentanglement of appearance and perspective in generative models. *Advances in Neural Information Processing Systems*, 32, 2019.
- [41] Higgins, I., L. Matthey, A. Pal, et al. beta-vae: Learning basic visual concepts with a constrained variational framework. In *International Conference on Learning Representations*. 2017.
- [42] Chen, R. T., X. Li, R. B. Grosse, et al. Isolating sources of disentanglement in variational autoencoders. In *Advances in Neural Information Processing Systems*, pages 2610–2620. 2018.
- [43] Kingma, D. P., M. Welling. Auto-encoding variational bayes. *arXiv preprint arXiv:1312.6114*, 2013.
- [44] Kingma, D. P., J. Ba. Adam: A method for stochastic optimization. In *International Conference on Learning Representations*. 2015.
- [45] Shi, F., B. Li, X. Xue. Raven’s progressive matrices completion with latent gaussian process priors. In *Proceedings of the AAAI Conference on Artificial Intelligence*, vol. 35, pages 9612–9620. 2021.
- [46] Gondal, M. W., M. Wuthrich, D. Miladinovic, et al. On the transfer of inductive bias from simulation to the real world: a new disentanglement dataset. *Advances in Neural Information Processing Systems*, 32, 2019.

- [47] Cattell, R. B. Theory of fluid and crystallized intelligence: A critical experiment. *Journal of educational psychology*, 54(1):1, 1963.
- [48] Raven, J. C., J. H. Court. *Raven's progressive matrices and vocabulary scales*, vol. 759. Oxford psychologists Press Oxford, 1998.

# Compositional Law Parsing with Latent Random Functions

## (Supplementary Materials)

Fan Shi Bin Li\* Xiangyang Xue

Shanghai Key Laboratory of Intelligent Information Processing

School of Computer Science, Fudan University

fshi22@m.fudan.edu.cn {libin, xyxue}@fudan.edu.cn

In Supplementary Materials, (1) we first provide the details of ELBO, then (2) introduce the datasets, model architecture, hyperparameters, and computational resources adopted in our experiments, and finally (3) provide additional experimental results. In particular, we provide additional results of *editing* and *manipulating* latent random functions, which well validate our motivation and contribution.

### A Details of ELBO

#### A.1 ELBO of Conditional Latent Variable Models

$$\begin{aligned}
 \log p(\mathbf{y}_T | \mathbf{y}_C, \mathbf{x}) &= \int_{\mathbf{h}} q(\mathbf{h} | \mathbf{y}, \mathbf{x}) \log p(\mathbf{y}_T | \mathbf{y}_C, \mathbf{x}) d\mathbf{h} \\
 &= \int_{\mathbf{h}} q(\mathbf{h} | \mathbf{y}, \mathbf{x}) \log \frac{p(\mathbf{h}, \mathbf{y}_T | \mathbf{y}_C, \mathbf{x})}{p(\mathbf{h} | \mathbf{y}, \mathbf{x})} d\mathbf{h} \\
 &= \int_{\mathbf{h}} q(\mathbf{h} | \mathbf{y}, \mathbf{x}) \log \frac{p(\mathbf{h}, \mathbf{y}_T | \mathbf{y}_C, \mathbf{x})}{q(\mathbf{h} | \mathbf{y}, \mathbf{x})} d\mathbf{h} + \int_{\mathbf{h}} q(\mathbf{h} | \mathbf{y}, \mathbf{x}) \log \frac{q(\mathbf{h} | \mathbf{y}, \mathbf{x})}{p(\mathbf{h} | \mathbf{y}, \mathbf{x})} d\mathbf{h} \quad (1) \\
 &\geq \int_{\mathbf{h}} q(\mathbf{h} | \mathbf{y}, \mathbf{x}) \log \frac{p(\mathbf{h}, \mathbf{y}_T | \mathbf{y}_C, \mathbf{x})}{q(\mathbf{h} | \mathbf{y}, \mathbf{x})} d\mathbf{h} \\
 &= \mathbb{E}_{q(\mathbf{h} | \mathbf{y}, \mathbf{x})} [\log p(\mathbf{y}_T | \mathbf{h})] - \mathbb{E}_{q(\mathbf{h} | \mathbf{y}, \mathbf{x})} \left[ \log \frac{q(\mathbf{h} | \mathbf{y}, \mathbf{x})}{p(\mathbf{h} | \mathbf{y}_C, \mathbf{x})} \right] = \mathcal{L}.
 \end{aligned}$$

#### A.2 Prior and Posterior Factorization

$$\begin{aligned}
 p(\mathbf{y}_T | \mathbf{h}) &= \prod_{t \in T} p(\mathbf{y}_t | \mathbf{z}_t) \\
 p(\mathbf{h} | \mathbf{y}_C, \mathbf{x}) &= \prod_{a \in A} p(f^a, \mathbf{z}_C^a, \mathbf{z}_T^a | \mathbf{y}_C, \mathbf{x}) \\
 &= \prod_{a \in A} p(\mathbf{z}_T^a | f^a, \mathbf{z}_C^a, \mathbf{x}_C, \mathbf{x}_T) p(f^a | \mathbf{z}_C^a, \mathbf{x}_C) p(\mathbf{z}_C^a | \mathbf{y}_C) \\
 &= \prod_{a \in A} \left( p(f^a | \mathbf{z}_C^a, \mathbf{x}_C) \prod_{t \in T} p(\mathbf{z}_t^a | f^a, \mathbf{z}_C^a, \mathbf{x}_C, \mathbf{x}_t) \prod_{c \in C} p(\mathbf{z}_c^a | \mathbf{y}_c) \right) \quad (2)
 \end{aligned}$$

\*Corresponding author

$$\begin{aligned}
q(\mathbf{h}|\mathbf{y}, \mathbf{x}) &= \prod_{a \in A} q(f^a, \mathbf{z}_C^a, \mathbf{z}_T^a | \mathbf{y}, \mathbf{x}) \\
&= \prod_{a \in A} q(f^a | \mathbf{z}^a, \mathbf{x}) q(\mathbf{z}_C^a | \mathbf{y}_C) q(\mathbf{z}_T^a | \mathbf{y}_T) \\
&= \prod_{a \in A} \left( q(f^a | \mathbf{z}^a, \mathbf{x}) \prod_{c \in C} q(\mathbf{z}_c^a | \mathbf{y}_c) \prod_{t \in T} q(\mathbf{z}_t^a | \mathbf{y}_t) \right)
\end{aligned} \tag{3}$$

### A.3 ELBO of CLAP

$$\begin{aligned}
\mathcal{L} &= \mathbb{E}_{q(\mathbf{h}|\mathbf{y}, \mathbf{x})} \left[ \log \prod_{t \in T} p(\mathbf{y}_t | \mathbf{z}_t) \right] \\
&\quad - \mathbb{E}_{q(\mathbf{h}|\mathbf{y}, \mathbf{x})} \left[ \log \frac{\prod_{a \in A} (q(f^a | \mathbf{z}^a, \mathbf{x}) \prod_{c \in C} q(\mathbf{z}_c^a | \mathbf{y}_c) \prod_{t \in T} q(\mathbf{z}_t^a | \mathbf{y}_t))}{\prod_{a \in A} (\prod_{t \in T} p(\mathbf{z}_t^a | f^a, \mathbf{z}_C^a, \mathbf{x}_C) p(f^a | \mathbf{z}_C^a, \mathbf{x}_C) \prod_{c \in C} p(\mathbf{z}_c^a | \mathbf{y}_c))} \right] \\
&= \sum_{t \in T} \mathbb{E}_{q(\mathbf{h}|\mathbf{y}, \mathbf{x})} [\log p(\mathbf{y}_t | \mathbf{z}_t)] - \sum_{a \in A} \mathbb{E}_{q(\mathbf{h}|\mathbf{y}, \mathbf{x})} \left[ \log \frac{\prod_{t \in T} q(\mathbf{z}_t^a | \mathbf{y}_t)}{\prod_{t \in T} p(\mathbf{z}_t^a | f^a, \mathbf{z}_C^a, \mathbf{x}_C, \mathbf{x}_t)} \right] \\
&\quad - \sum_{a \in A} \mathbb{E}_{q(\mathbf{h}|\mathbf{y}, \mathbf{x})} \left[ \log \frac{q(f^a | \mathbf{z}^a, \mathbf{x})}{p(f^a | \mathbf{z}_C^a, \mathbf{x}_C)} \right] - \sum_{a \in A} \mathbb{E}_{q(\mathbf{h}|\mathbf{y}, \mathbf{x})} \left[ \log \frac{\prod_{c \in C} q(\mathbf{z}_c^a | \mathbf{y}_c)}{\prod_{c \in C} p(\mathbf{z}_c^a | \mathbf{y}_c)} \right] \\
&= \underbrace{\sum_{t \in T} \mathbb{E}_{q(\mathbf{h}|\mathbf{y}, \mathbf{x})} [\log p(\mathbf{y}_t | \mathbf{z}_t)]}_{\text{Reconstruction term } \mathcal{L}_r} - \underbrace{\sum_{a \in A} \sum_{t \in T} \mathbb{E}_{q(\mathbf{h}|\mathbf{y}, \mathbf{x})} \left[ \log \frac{q(\mathbf{z}_t^a | \mathbf{y}_t)}{p(\mathbf{z}_t^a | f^a, \mathbf{z}_C^a, \mathbf{x}_C, \mathbf{x}_t)} \right]}_{\text{Target regularizer } \mathcal{L}_t} \\
&\quad - \underbrace{\sum_{a \in A} \mathbb{E}_{q(\mathbf{h}|\mathbf{y}, \mathbf{x})} \left[ \log \frac{q(f^a | \mathbf{z}^a, \mathbf{x})}{p(f^a | \mathbf{z}_C^a, \mathbf{x}_C)} \right]}_{\text{Function regularizer } \mathcal{L}_f} - \underbrace{\sum_{a \in A} \sum_{c \in C} \mathbb{E}_{q(\mathbf{h}|\mathbf{y}, \mathbf{x})} \left[ \log \frac{q(\mathbf{z}_c^a | \mathbf{y}_c)}{p(\mathbf{z}_c^a | \mathbf{y}_c)} \right]}_{\text{Context regularizer } \mathcal{L}_c}
\end{aligned} \tag{4}$$

#### A.3.1 Reconstruction Term

$$\begin{aligned}
\mathcal{L}_r &= \sum_{t \in T} \mathbb{E}_{q(\mathbf{h}|\mathbf{y}, \mathbf{x})} [\log p(\mathbf{y}_t | \mathbf{z}_t)] = \sum_{t \in T} \mathbb{E}_{q(\mathbf{z}_t | \mathbf{y}_t)} [\log p(\mathbf{y}_t | \mathbf{z}_t)] \\
&\approx \sum_{t \in T} \log p(\mathbf{y}_t | \tilde{\mathbf{z}}_t), \quad \text{where } \tilde{\mathbf{z}}_t \sim q(\mathbf{z}_t | \mathbf{y}_t)
\end{aligned} \tag{5}$$

#### A.3.2 Target Regularizer

$$\begin{aligned}
\mathcal{L}_t &= \sum_{a \in A} \sum_{t \in T} \mathbb{E}_{q(\mathbf{h}|\mathbf{y}, \mathbf{x})} \left[ \log \frac{q(\mathbf{z}_t^a | \mathbf{y}_t)}{p(\mathbf{z}_t^a | f^a, \mathbf{z}_C^a, \mathbf{x}_C, \mathbf{x}_t)} \right] \\
&= \sum_{a \in A} \sum_{t \in T} \mathbb{E}_{q(\mathbf{z}_C^a | \mathbf{y}_C)} \left[ \mathbb{E}_{q(\mathbf{z}_T^a | \mathbf{y}_T)} \left[ \mathbb{E}_{q(f^a | \mathbf{z}^a, \mathbf{x})} \left[ \log \frac{q(\mathbf{z}_t^a | \mathbf{y}_t)}{p(\mathbf{z}_t^a | f^a, \mathbf{z}_C^a, \mathbf{x}_C, \mathbf{x}_t)} \right] \right] \right].
\end{aligned} \tag{6}$$

Because of the function consistency in samples, function posteriors  $q(f^a | \tilde{\mathbf{z}}^a, \mathbf{x})$  derived from arbitrary sampled  $\tilde{\mathbf{z}}^a \sim q(\mathbf{z}^a | \mathbf{y})$  need to be consistent. So we let  $f^a$  condition on only the observations  $\mathbf{x}$  and  $\mathbf{y}$  to simplify the posterior distribution, that is, we replace  $q(f^a | \tilde{\mathbf{z}}^a, \mathbf{x})$  with  $q(f^a | \mathbf{y}, \mathbf{x})$ :

$$\begin{aligned}
\mathcal{L}_t &\approx \sum_{a \in A} \sum_{t \in T} \mathbb{E}_{q(\mathbf{z}_C^a | \mathbf{y}_C)} \left[ \mathbb{E}_{q(\mathbf{z}_T^a | \mathbf{y}_T)} \left[ \mathbb{E}_{q(f^a | \mathbf{y}, \mathbf{x})} \left[ \log \frac{q(\mathbf{z}_t^a | \mathbf{y}_t)}{p(\mathbf{z}_t^a | f^a, \mathbf{z}_C^a, \mathbf{x}_C, \mathbf{x}_t)} \right] \right] \right] \\
&= \sum_{a \in A} \sum_{t \in T} \mathbb{E}_{q(\mathbf{z}_C^a | \mathbf{y}_C)} \left[ \mathbb{E}_{q(f^a | \mathbf{y}, \mathbf{x})} \left[ \text{KL}(q(\mathbf{z}_t^a | \mathbf{y}_t) \| p(\mathbf{z}_t^a | f^a, \mathbf{z}_C^a, \mathbf{x}_C, \mathbf{x}_t)) \right] \right].
\end{aligned} \tag{7}$$

In this way, we convert the computation of the log-likelihoods on  $q(\mathbf{z}_t^a | \mathbf{y}_t)$  and  $p(\mathbf{z}_t^a | f^a, \mathbf{z}_C^a, \mathbf{x}_C, \mathbf{x}_t)$  to the KL divergences between them. Then a Monte Carlo estimator can be used to approximate

$\mathcal{L}_t$  where  $\tilde{z}_C^a$  is sampled by  $\tilde{z}_C^a \sim q(z_C^a | \mathbf{y}_C)$  to compute the outer expectation  $\mathbb{E}_{q(z_C^a | \mathbf{y}_C)}[\cdot]$ ; and for inner expectation  $\mathbb{E}_{q(f^a | \mathbf{y}, \mathbf{x})}[\cdot]$ , because  $q(f^a | \mathbf{y}, \mathbf{x}) = \int q(f^a | \mathbf{z}^a, \mathbf{x}) q(\mathbf{z}^a | \mathbf{x}) d\mathbf{z}^a$ , we are able to first sample  $\tilde{z}_T^a \sim q(z_T^a | \mathbf{y}_T)$  and obtain  $\tilde{f}^a \sim q(f^a | \tilde{z}_C^a, \tilde{z}_T^a, \mathbf{x})$ . By means of  $\tilde{f}^a$  and  $\tilde{z}^a$  sampled from the posterior, we have  $\mathcal{L}_t \approx \text{KL}(q(z_t^a | \mathbf{y}_t) \| p(z_t^a | \tilde{f}^a, \tilde{z}_C^a, \mathbf{x}_C, \mathbf{x}_t))$ .

### A.3.3 Function Regularizer

$$\begin{aligned} \mathcal{L}_f &= \sum_{a \in A} \mathbb{E}_{q(\mathbf{h} | \mathbf{y}, \mathbf{x})} \left[ \log \frac{q(f^a | \mathbf{z}^a, \mathbf{x})}{p(f^a | \mathbf{z}_C^a, \mathbf{x}_C)} \right] \\ &= \sum_{a \in A} \mathbb{E}_{q(z_C^a | \mathbf{y}_C)} \left[ \mathbb{E}_{q(z_T^a | \mathbf{y}_T)} \left[ \mathbb{E}_{q(f^a | \mathbf{z}^a, \mathbf{x})} \left[ \log \frac{q(f^a | \mathbf{z}^a, \mathbf{x})}{p(f^a | \mathbf{z}_C^a, \mathbf{x}_C)} \right] \right] \right] \\ &= \sum_{a \in A} \mathbb{E}_{q(\mathbf{z}^a | \mathbf{y})} \left[ \text{KL}(q(f^a | \mathbf{z}^a, \mathbf{x}) \| p(f^a | \mathbf{z}_C^a, \mathbf{x}_C)) \right]. \end{aligned} \quad (8)$$

To estimate  $\mathcal{L}_f$  in the same way as the target regularizer,  $\tilde{z}^a$  is sampled by  $\tilde{z}^a \sim q(\mathbf{z}^a | \mathbf{y})$  and we have  $\mathcal{L}_f \approx \text{KL}(q(f^a | \tilde{z}^a, \mathbf{x}) \| p(f^a | \tilde{z}_C^a, \mathbf{x}_C))$ .

### A.3.4 Context Regularizer

$$\mathcal{L}_c = \sum_{a \in A} \sum_{c \in C} \mathbb{E}_{q(\mathbf{h} | \mathbf{y}, \mathbf{x})} \left[ \log \frac{q(z_c^a | \mathbf{y}_c)}{p(z_c^a | \mathbf{y}_c)} \right] = \sum_{a \in A} \sum_{c \in C} \mathbb{E}_{q(\mathbf{h} | \mathbf{y}, \mathbf{x})} [\log 1] = 0. \quad (9)$$

## A.4 Total Correlation

Let  $\mathcal{I} = \{\mathbf{y}_1, \dots, \mathbf{y}_K\}$  be the set with images from all samples in the dataset, and  $\tilde{\mathbf{z}}_k \sim q(\mathbf{z}_k | \mathbf{y}_k)$  are the sampled latent variables for each image. To apply the Total Correlation (TC) of  $\beta$ -TCVAE [1] to CLAP, we make a tiny modification that the aggregated posterior  $\bar{q}(\mathbf{z}) = \sum_{k=1}^K q(\mathbf{z}_k | \mathbf{y}_k) p(\mathbf{y}_k)$  is decomposed along with concepts instead of the dimension of latent variables. According to  $\beta$ -TCVAE, there is

$$\mathcal{R}_{TC} = \text{KL} \left( \bar{q}(\mathbf{z}) \left\| \prod_{a \in A} \bar{q}(\mathbf{z}^a) \right. \right) = \mathbb{E}_{\bar{q}(\mathbf{z})} [\log \bar{q}(\mathbf{z})] - \sum_{a \in A} \mathbb{E}_{\bar{q}(\mathbf{z})} [\log \bar{q}(\mathbf{z}^a)]. \quad (10)$$

where  $\beta$ -TCVAE provides Minibatch Weighted Sampling (MWS) to approximate Equation 10 by a minibatch  $\{\mathbf{y}_m | m \in M\} \subseteq \mathcal{I}$  of the dataset:

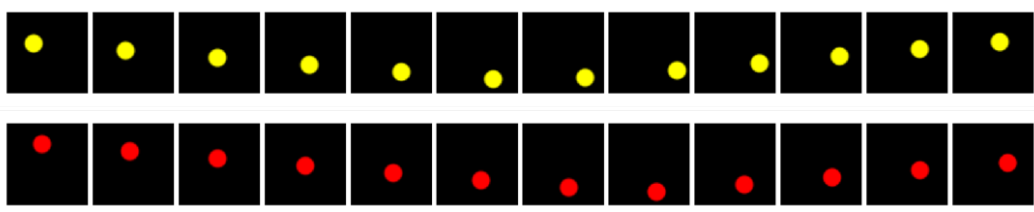
$$\begin{aligned} \mathbb{E}_{\bar{q}(\mathbf{z})} [\log \bar{q}(\mathbf{z})] &\approx \frac{1}{|M|} \sum_{i \in M} \left[ \log \sum_{j \in M} q(\tilde{\mathbf{z}}_i | \mathbf{y}_j) - \log(K|M) \right] \\ \mathbb{E}_{\bar{q}(\mathbf{z})} [\log \bar{q}(\mathbf{z}^a)] &\approx \frac{1}{|M|} \sum_{i \in M} \left[ \log \sum_{j \in M} q(\tilde{\mathbf{z}}_i^a | \mathbf{y}_j) - \log(K|M) \right]. \end{aligned} \quad (11)$$

## B Datasets and Experimental Setup

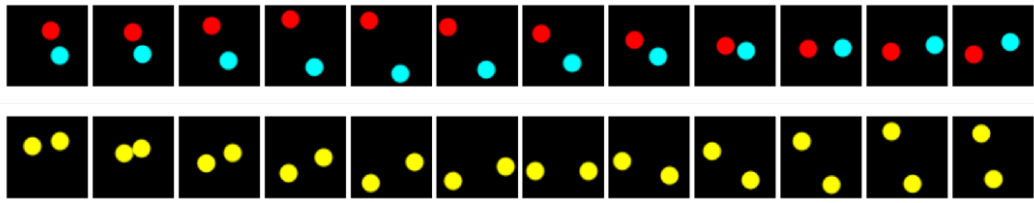
### B.1 Details of Datasets

In this paper, three types of datasets are adopted: BoBa, CRPM, and MPI3D. Figure 1 displays two samples for each instance of the datasets, and Table 1 describes the train, validation, and test configurations of the instances.

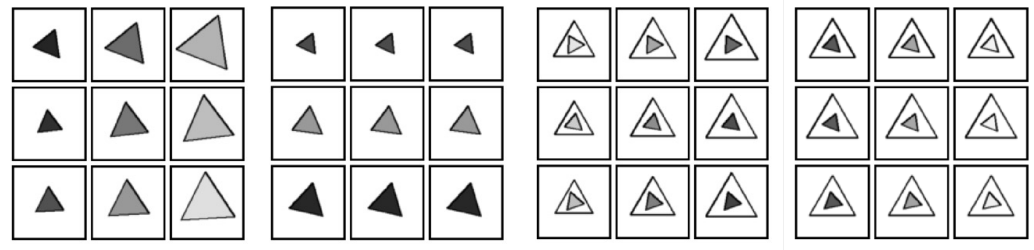
**Bouncing Ball (BoBa)** BoBa contains many videos of bouncing balls. Depending on the number of balls in the scene, the dataset provides two instances BoBa-1 and BoBa-2. In the videos of Figure 1a and 1b, the motion of balls follows the law of physical collisions; and the appearance of balls (color, size, amount, etc.) is constant over time. The models need to capture the probability space on functions  $f : \mathbb{R} \mapsto \mathbb{R}^{3 \times 64 \times 64}$  that map timestamps to video frames. Referring to Table 1, we provide



(a) BoBa-1

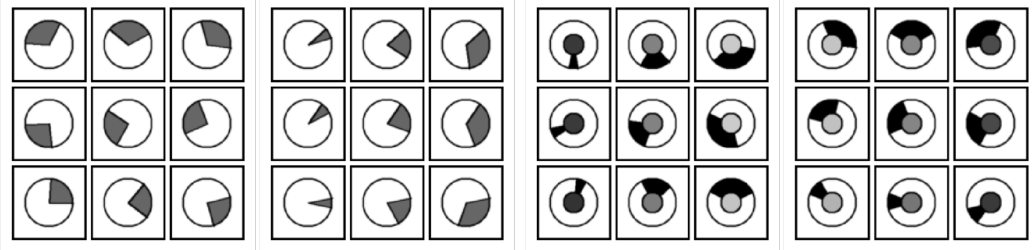


(b) BoBa-2



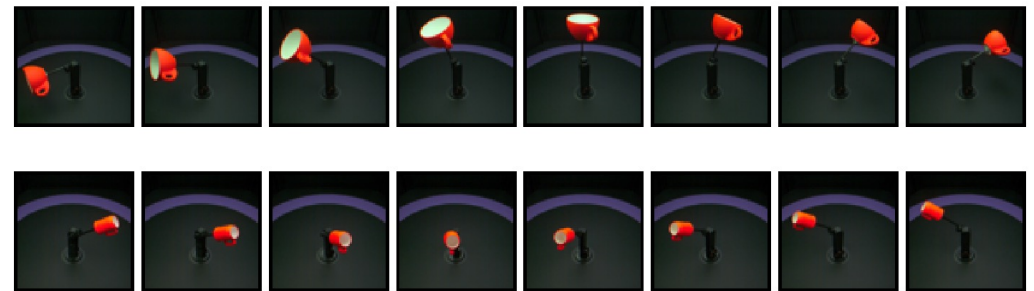
(c) CRPM-triangle

(d) CRPM-double-triangle



(e) CRPM-circle

(f) CRPM-double-circle



(g) MPI3D

Figure 1: Examples from the different instances of datasets: (a) BoBa-1 and (b) BoBa-2 are instances of BoBa; (c) triangle, (d) double-triangle, (e) circle, and (f) double-circle are instances of CRPM; (g) is MPI3D.



Table 1: Details of BoBa, CRPM, and MPI3D dataset. Row 1: dataset names. Row 2: splits of datasets where the number  $k$  in the suffix of Test- $k$  denotes the number of target images. Row 3: number of samples in each split. Row 4: number of images in each sample. Row 5: number of target images in a sample. Row 6: image size represented by Channel  $\times$  Height  $\times$  Width.

Dataset	BoBa-1				BoBa-2			
Split	Train	Valid	Test-2	Test-4	Train	Valid	Test-2	Test-4
Samples	10000	1000	2000	2000	10000	1000	2000	2000
Images	12				12			
Targets	1 ~ 4	1 ~ 4	2	4	1 ~ 4	1 ~ 4	2	4
Image Size	3 × 64 × 64				3 × 64 × 64			
Dataset	CRPM-triangle				CRPM-circle			
Split	Train	Valid	Test-2	Test-3	Train	Valid	Test-2	Test-3
Samples	10000	1000	2000	2000	10000	1000	2000	2000
Images	9				9			
Targets	1 ~ 2	1 ~ 2	2	3	1 ~ 2	1 ~ 2	2	3
Image Size	64 × 64				64 × 64			
Dataset	CRPM-double-triangle				CRPM-double-circle			
Split	Train	Valid	Test-2	Test-3	Train	Valid	Test-2	Test-3
Samples	10000	1000	2000	2000	10000	1000	2000	2000
Images	9				9			
Targets	1 ~ 2	1 ~ 2	2	3	1 ~ 2	1 ~ 2	2	3
Image Size	64 × 64				64 × 64			
Dataset	MPI3D							
Split	Train	Valid	Test-2	Test-5	Test-10	Test-20		
Samples	16127	2305	4608	4608	4608	4608	4608	
Images	8					40		
Targets	1 ~ 4	1 ~ 4	2	5	10	20		
Image Size	3 × 64 × 64							

10,000 videos of bouncing balls for training, 1,000 for validation and hyperparameter selection, and 2,000 to test the intuitive physics of the models. In the training and validation phase, we randomly select 1 to 4 frames from video frames as the target images to predict; in the testing phase, we provide two configurations (referred to as Test-2 and Test-4) to evaluate the model’s performance when there are 2 and 4 target images in videos.

**Continuous Raven’s Progressive Matrix (CRPM)** CRPM consists of  $3 \times 3$  image matrices where the images contain one or two centered triangles or circles. CRPM provides four instances with different image types: triangle, double-triangle, circle, and double-circle. Images in a matrix follow attribute-specific changing rules (e.g., rules in the size, grayscale, and rotation of the triangle). The first sample in Figure 1c shows that, for images within the row, the sizes of triangles increase progressively, the grayscales change progressively from dark to light, and the rotations keep constant. To predict the missing target images in the matrix, the models need to learn the probability space on functions  $f : \{-1, 0, 1\}^2 \mapsto \mathbb{R}^{64 \times 64}$  that map 2D grid coordinates to grid images. Table 1 shows that we provide 10,000 image matrices for training, 1,000 for tuning the model hyperparameters, and 2,000 to test the abstract visual reasoning ability of models. In the training and validation process, we randomly select 1 or 2 images as target images; in the testing process, we use Test-2 and Test-3 to evaluate the performance of the models to predict 2 and 3 target images.

Table 2: Hyperparameters of CLAP-NP where lr = learning rate, bs = batch size, and anneal is the annealing step to reach the maximum value of  $\beta_t$  and  $\beta_f$ .

Hyperparameter	$d_A$	$ A $	$H_a$	$L_a$	$d_a$	$H_f$	$L_f$	$d_g$	$H_p$	$L_p$
BoBa-1	1	3	256	2	64	128	1	32	128	2
BoBa-2	1	6	256	2	256	256	1	128	256	2
CRPM-triangle	1	3	256	2	128	128	2	64	128	2
CRPM-double-triangle	1	3	256	2	128	128	2	64	128	2
CRPM-cricle	1	2	256	2	128	128	1	64	128	2
CRPM-double-circle	1	3	256	2	128	128	1	64	128	2
MPI3D	1	8	128	2	64	64	1	64	128	1

Hyperparameter	lr	bs	$\beta_t$	$\beta_f$	anneal	$\beta_{TC}$	$\sigma_z$	$\sigma_x$
BoBa-1	0.0003	512	100	100	N/A	1000	0.03	0.1
BoBa-2	0.0003	512	400	100	N/A	1500	0.03	0.1
CRPM-triangle	0.0003	512	400	200	N/A	5000	0.1	0.1
CRPM-double-triangle	0.0003	512	200	50	N/A	5000	0.1	0.1
CRPM-cricle	0.0003	512	100	100	N/A	5000	0.1	0.1
CRPM-double-circle	0.0003	512	300	300	N/A	5000	0.1	0.1
MPI3D	0.0005	512	50	50	400	100	0.03	0.1

**MPI3D** MPI3D [2] dataset contains a series of single-object scenes, each with 40 different scene images. There are two underlying rules to change the object in a scene: change the altitude of the object (sample 1 in Figure 1g); change the azimuth of the object (sample 2 in Figure 1g). The other attributes (e.g., object color, camera height, etc.) do not change within scene images. It is essential for the models to grasp different changing patterns for target image prediction, and the key is to describe the distribution over functions  $f : \mathbb{R} \mapsto \mathbb{R}^{3 \times 64 \times 64}$  that map object altitudes or azimuths to scene images. As Table 1 shows, we provide 16127 scenes for training, 2305 for tuning the hyperparameters, and 4608 for testing. In terms of training and validation, we first randomly select 8 images from 40 scene images to represent the scene, and then randomly select 1 to 4 images from the 8 images again as the target images, leaving the remaining 7 to 4 images as the context. For testing, we supply Test-2, Test-5, Test-10 and Test-20, where Test-2 and Test-5 evaluate the performance of the models to predict 2 and 3 target images out of 8 images; Test-10 and Test-20 evaluate the performance to predict 10 and 20 target images out of 40 images. One can fetch MPI3D from the repository <sup>2</sup> under the Creative Commons Attribution 4.0 International License.

## B.2 Model Architecture and Hyperparameters

**CLAP-NP** In this subsection, we will first describe the architecture of the encoder, decoder, concept-specific function parsers and concept-specific target predictors network in CLAP-NP; and then list the hyperparameters in the training phase.

- **Encoder:** for all datasets, CLAP-NP uses the same convolutional blocks to downsample high-dimensional images into parameters of concepts, which can be described as
  - $4 \times 4$  Conv, stride 2, padding 1, 32 BatchNorm, ReLU
  - $4 \times 4$  Conv, stride 2, padding 1, 32 BatchNorm, ReLU
  - $4 \times 4$  Conv, stride 2, padding 1, 64 BatchNorm, ReLU
  - $4 \times 4$  Conv, stride 2, padding 1, 128 BatchNorm, ReLU
  - $4 \times 4$  Conv, 256 BatchNorm, ReLU
  - $1 \times 1$  Conv, 512
  - ReshapeBlock, 512
  - Fully Connected,  $d_A|A|$

where  $d_A$  is the size of each concept  $a \in A$ . The ReshapeBlock flattens the output tensor of size  $512 \times 1 \times 1$  from the last convolutional layer to the vector of size 512. The output of the encoder is the mean of the  $|A|$  visual concepts of size  $d_A$ .

<sup>2</sup>[https://github.com/rr-learning/disentanglement\\_dataset](https://github.com/rr-learning/disentanglement_dataset)

- **Decoder:** In BoBa and CRPM datasets, CLAP-NP uses several deconvolutional layers to upsample concepts to images, which is

- ReshapeBlock,  $d_A|A| \times 1 \times 1$
- $1 \times 1$  Deconv, 128 BatchNorm, ReLU
- $4 \times 4$  Deconv, 64 BatchNorm2d, ReLU
- $4 \times 4$  Deconv, stride 2, padding 1, 32 BatchNorm, ReLU
- $4 \times 4$  Deconv, stride 2, padding 1, 32 BatchNorm, ReLU
- $4 \times 4$  Deconv, stride 2, padding 1, 32 BatchNorm, ReLU
- $4 \times 4$  Deconv, stride 2, padding 1,  $N_C$  Sigmoid

where  $N_C$  is the number of image channels and Sigmoid is the activation function used to generate pixel values ranging in  $(0, 1)$ . To generate more complex scene images in MPI3D, CLAP-NP uses the ConvLSTM decoder in GQN [3] where the number of iterations is set to 4, the size of iteration outputs is 64, and the ConvLSTM core is shared among iterations.

- **Function Parser:** CLAP-NP provides identical but independent function parsers for each concept. Each function parser consists of a multi-layer perception (MLP)  $\mathcal{T}_c$  to encode concepts, a MLP  $\mathcal{T}_i$  to encode function inputs, a MLP  $\mathcal{T}_a$  to aggregate context points, and a MLP  $\mathcal{T}_f$  to predict the mean and standard deviation of the global latent variable. The architecture of  $\mathcal{T}_c$  and  $\mathcal{T}_i$  is

- Fully Connected, 32 ReLU
- Fully Connected, 16

By concatenating the encoded concepts and the encoded function inputs, we get the context function points. The architecture of  $\mathcal{T}_a$  is

- [ Fully Connected,  $H_a$  ReLU ]  $\times L_a$
- Fully Connected,  $d_a$

where  $H_a$  and  $L_a$  represent the hidden size and the number of layers in  $\mathcal{T}_a$ , and  $d_a$  is the aggregate size. Finally, the architecture of  $\mathcal{T}_f$  is

- [ Fully Connected,  $H_f$  ReLU ]  $\times L_f$
- Fully Connected,  $2d_g$

where  $H_f$  and  $L_f$  represent the hidden size and the number of layers in  $\mathcal{T}_f$ , and  $d_g$  is the size of the global latent variable  $\mathbf{g}^a$ . The outputs of  $\mathcal{T}_f$  consist of the mean and standard deviation of  $\mathbf{g}^a$ .

- **Target Predictor:** the concept-specific target predictor  $\mathcal{T}_p$  is a MLP that maps  $\mathbf{g}^a$  and the encoded function input into the target concept, whose architecture is

- [ Fully Connected,  $H_p$  ReLU ]  $\times L_p$
- Fully Connected,  $d_A$

where  $H_p$  and  $L_p$  represent the hidden size and the number of layers in  $\mathcal{T}_p$ .

Hyperparameters for CLAP-NP on different datasets are shown in Table 2. After each training epoch, we use the validation set to compute evidence lower bound (ELBO) of the current model and save the model with the largest ELBO as the trained model. For all datasets, CLAP-NP uses the Adam [4] optimizer to update parameters.

**Neural Process (NP)** Different from [5], to apply NP in high-dimensional images, we add an encoder and decoder which are the same as those in CLAP-NP to convert high-dimensional images into low-dimensional representations. And the representations are combined with the function inputs to form the context by an aggregator  $\mathcal{T}_a$ . Then the function parser  $\mathcal{T}_f$  obtains the mean and standard deviation of the global latent variable. Finally, the decoder generates target images from the target function inputs and the global latent variable. The architectures of  $\mathcal{T}_a$  and  $\mathcal{T}_f$  are

- **Aggregator**
  - Fully Connected, 512 ReLU
  - Fully Connected, 512 ReLU
  - Fully Connected, 512
- **Function Parser**
  - Fully Connected, 512 ReLU

Table 3: MSEs on CRPM-triangle and CRPM-circle

Model	CRPM-triangle		CRPM-circle	
	MSE-2	MSE-3	MSE-2	MSE-3
NP	$0.3146 \pm 0.0188$	$0.4928 \pm 0.0311$	$0.2583 \pm 0.0199$	$0.4551 \pm 0.0410$
GQN	$0.9733 \pm 0.0328$	$1.9890 \pm 0.0922$	$0.9974 \pm 0.0381$	$1.9478 \pm 0.0875$
CLAP-NP	<b><math>0.0873 \pm 0.0061</math></b>	<b><math>0.1569 \pm 0.0585</math></b>	<b><math>0.1322 \pm 0.0675</math></b>	<b><math>0.2952 \pm 0.0781</math></b>

- Fully Connected, 512 ReLU
- Fully Connected, 1024

For all datasets, NP adopts the learning rate 0.0001, representation of size 16, batch size 512, and  $\sigma_x = 0.1$ . We select the final model by ELBO on the validation set. For all datasets, NP uses the Adam optimizer for parameter updates.

**Generative Query Network (GQN)** To implement GQN [3], we use a PyTorch implementation from the repository <sup>3</sup> with the following changes to the default configuration: set learning rate to 0.0005; set batch size to 256; set the representation type to pool; set the number of iterations to 4; and share the ConvLSTM core among iterations. The selection of the saved model is still based on ELBO on the validation set.

### B.3 Computational Resource

We train our model and baselines on two servers: (1) the server with Intel(R) Xeon(R) E5-2630 v4 CPUs, 12GB NVIDIA TITAN Xp GPUs, 256GB RAM and Ubuntu 16.04 OS; (2) the server with Intel(R) Xeon(R) Gold 6133 CPUs, 24GB NVIDIA GeForce RTX 3090 GPUs, 512GB RAM and Ubuntu 18.04 OS. Tasks that require less memory size of GPUs, such as training CLAP-NP on BoBa and CRPM and training NP on all three datasets, are performed on the first server. Because of the ConvLSTM architecture, training GQN on all three datasets and training CLAP-NP on MPI3D have higher computation and memory overhead. So we perform these tasks on the second server. All models are implemented with the PyTorch [6] framework. To avoid the randomness in dataset splitting, we fix the random seed to 0.

## C Additional Experimental Results

**Intuitive Physics** In Figure 2 we display additional prediction results on BoBa-1 and BoBa-2. For each instance, there are two samples that correspond to Test-2 and Test-4, where CLAP-NP outperforms other baselines. NP generates blurred target images on both BoBa-1 and BoBa-2 datasets. It indicates that NP has difficulty modeling changing patterns on bouncing balls. GQN can generate clear images, but has two drawbacks: in sample 1 of BoBa-1 and sample 2 of BoBa-2, GQN generates the non-existent ball; in sample 2 of BoBa-1 and sample 1 of BoBa-2, the predictions of GQN deviate from the ground truths significantly in the position of balls. Overall, CLAP-NP performs well in both modeling scene consistency and predicting motion trajectory.

**Abstract Visual Reasoning** With the additional experimental results in Figure 3, we can intuitively see that CLAP-NP has a better understanding of the changing rules than baselines. For the second sample of each dataset, a row of images is removed to interpret the abstract visual reasoning ability of the model. As sample 2 in Figure 3a shows, when we remove a row of images, the answer is not unique: the predictions are correct as long as their sizes increase progressively and their colors and rotations keep constant. CLAP-NP represents such randomness in predictions by means of the probabilistic generative process, making it possible to generate different correct answers. In terms of the prediction quality, although generating blurred images, NP has the basic reasoning ability about the progressive rule of the outer triangle size in sample 1 of Figure 3b. GQN generates clear images, however, on CRPM-circle and CRPM-double-circle the generated images can hardly follow the underlying changing rules on matrices. Table 3 illustrates the outperforming results of CLAP-NP in abstract visual reasoning by quantitative experiments.

<sup>3</sup><https://github.com/iShohei220/torch-gqn>

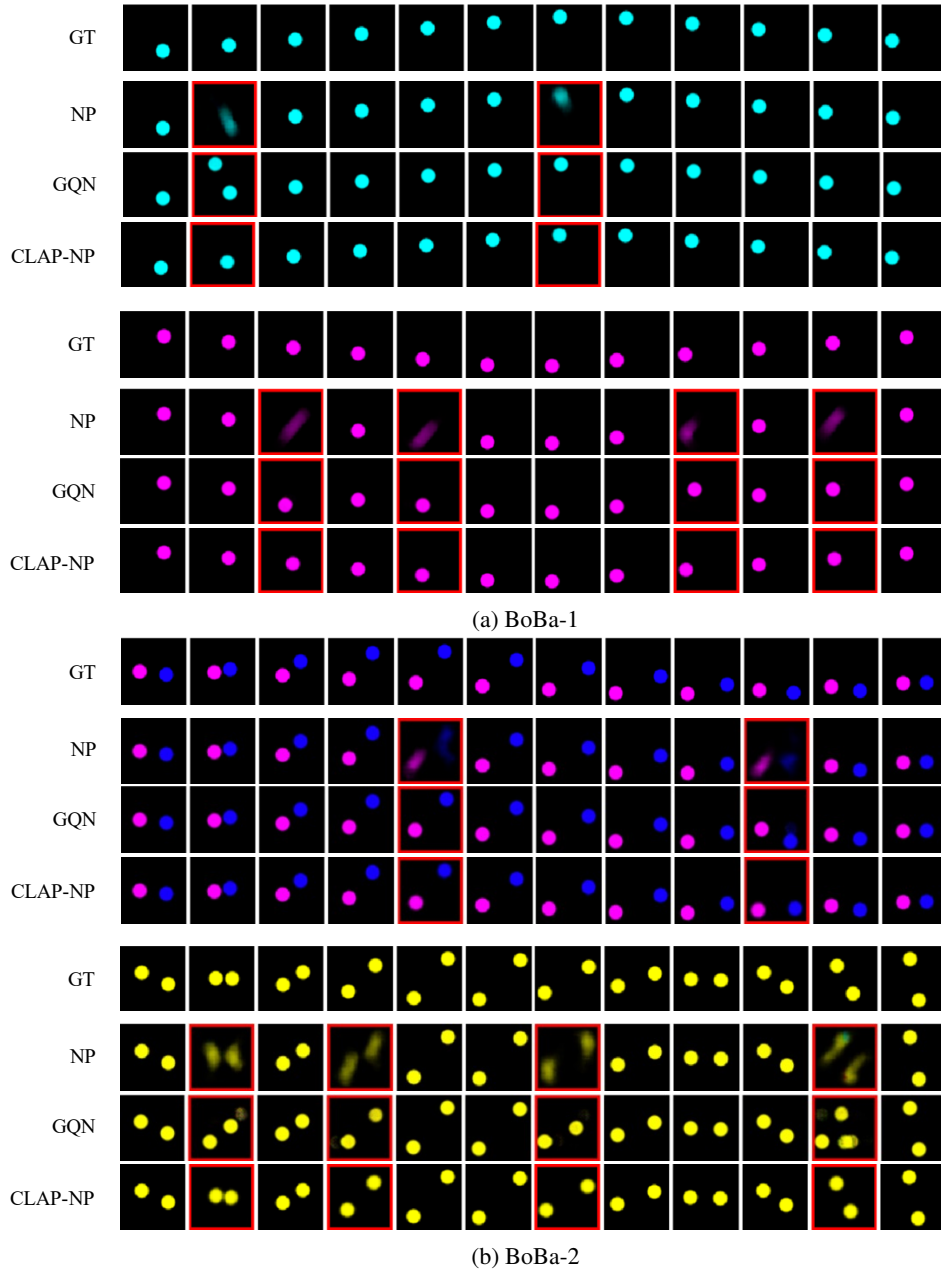
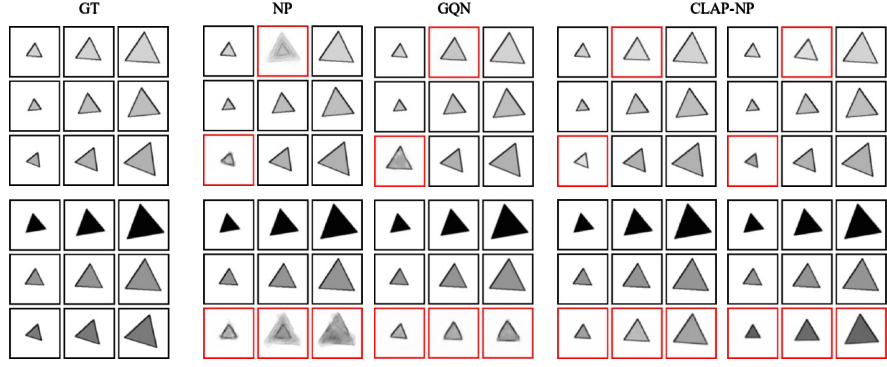
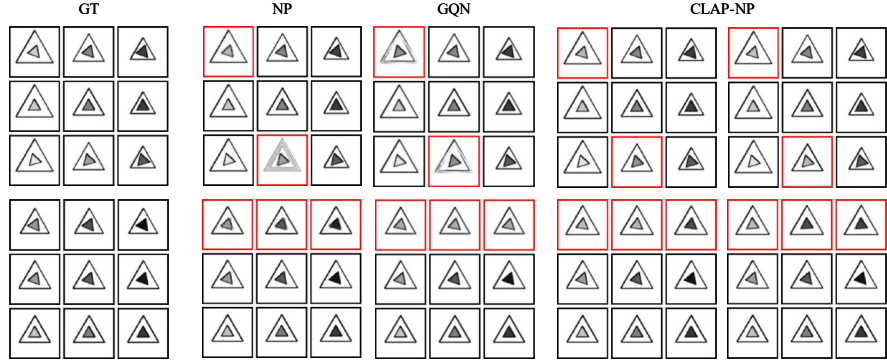


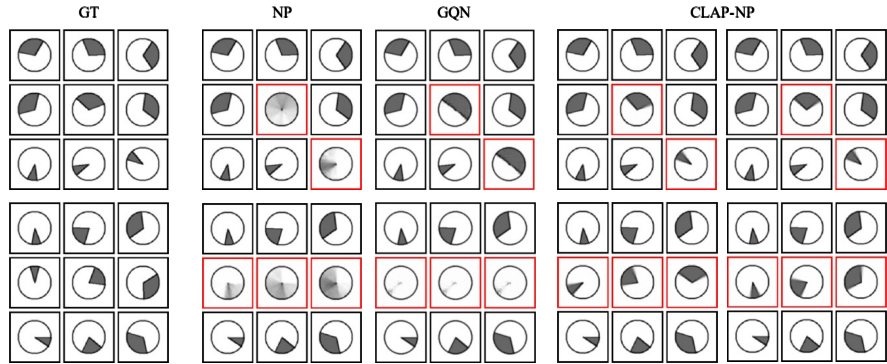
Figure 2: Prediction results on BoBa. The images with red boxes are prediction results of models.



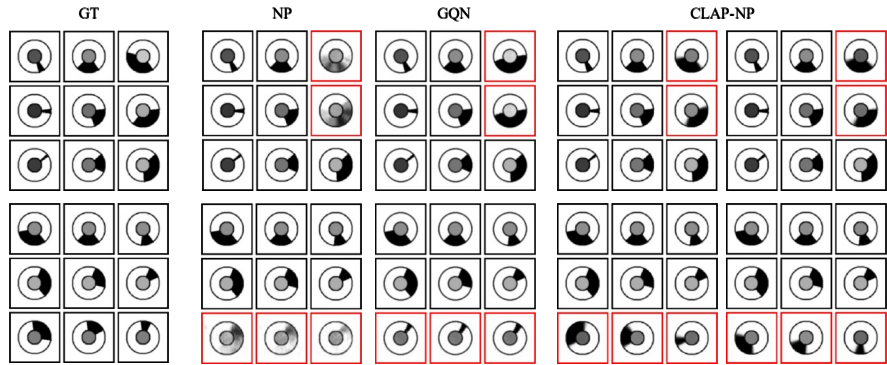
(a) CRPM-triangle



(b) CRPM-double-triangle



(c) CRPM-circle



(d) CRPM-double-circle

Figure 3: Predictions on CRPM. For each sample, we show two predictions sampled from CLAP-NP and one from each baseline to demonstrate the model’s understanding of the attribute-specific rules.

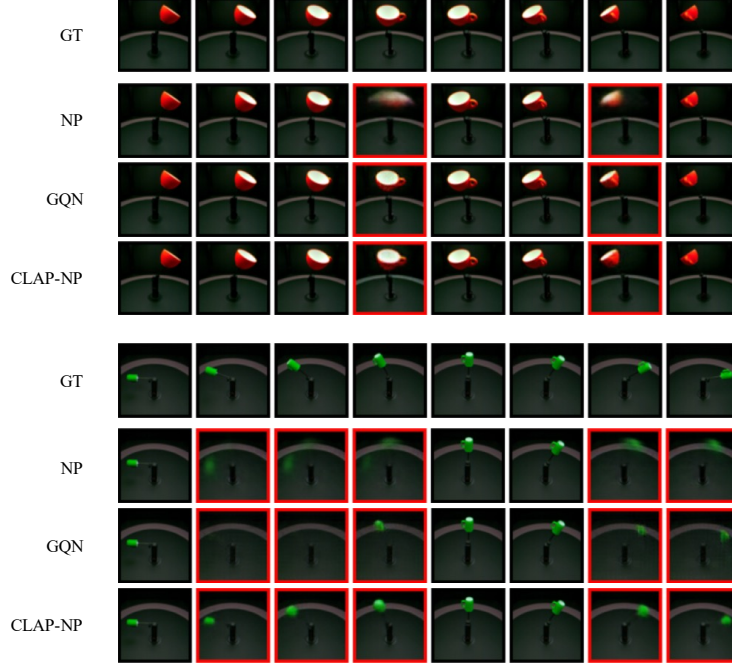


Figure 4: Target prediction with 8 scene images on MPI3D

**Scene Representation** Figure 4 shows the prediction results within 8 scene images. Both GQN and CLAP-NP generate high-quality prediction results when the number of target images is 2; if the number of target images is increased to 5, the prediction results of GQN have significant deviations, while CLAP-NP maintains the accuracy of predictions. NP generates ambiguous results in all experiments. Figure 5 shows a more complicated situation: we provide 40 scene images and set 20 of them as target images. In this case, GQN and NP can hardly generate clear foreground objects; while CLAP-NP produces relatively accurate predictions with only a little decrease in generative quality. This experiment aims to test the generalization of the laws learned by the models, and the results above illustrate that NP can hardly represent scenes with functions, GQN has difficulty generalizing the scene representation ability to different configurations, and the laws learned by CLAP-NP can be generalized to novel scenes with more available images.

**Concept Decomposition** Concept decomposition is the foundation for CLAP to understand concept-specific laws. In this experiment, we traverse each concept in the latent space and visualize the concepts through a decoder to illustrate the meaning of each concept. First of all, we decompose a batch of images into concepts by the encoder to estimate the range of concepts in the latent space. To traverse one concept, we fix the other concepts and linearly interpolate it from the minimum value to the maximum value to generate a sequence of interpolation results, which are decoded into images for visualization. Each row of Figure 6 represents the traversal results of one concept. In BoBa-1, CLAP-NP decomposes images into concepts of color, horizontal position, and vertical position in an unsupervised manner. This is similar to the way we understand the motion of balls: the color keeps constant over time; the horizontal and vertical positions conform to the physical laws in their respective directions. As Figure 6a shows, the concept decomposition in BoBa-2 is more complex, where the color of two balls is encoded by two concepts (the 2nd and 6th row), and the horizontal/vertical position is described by the concept in row 1/4, and the remaining concepts represent the relative position between two balls. In CRPM, CLAP-NP correctly parses images into concepts that correspond to the attribute-specific rules in matrices. With the example of CRPM-circle in Figure 6b, the size and rotation of the sectors follow the progressive changing rule or constant rule independently, while CLAP-NP has the ability to decompose the size and rotation of the sectors as concepts. Concept decomposition in real environments is a challenge for models. In MPI3D, CLAP-NP parses the scene images into the object altitudes (1st row), object azimuths (4th row), camera heights (6th row), and object colors (7th row). In the first row of Figure 6c, the object altitude is slightly entangled with the object shape, which shows that there is still room for our model to

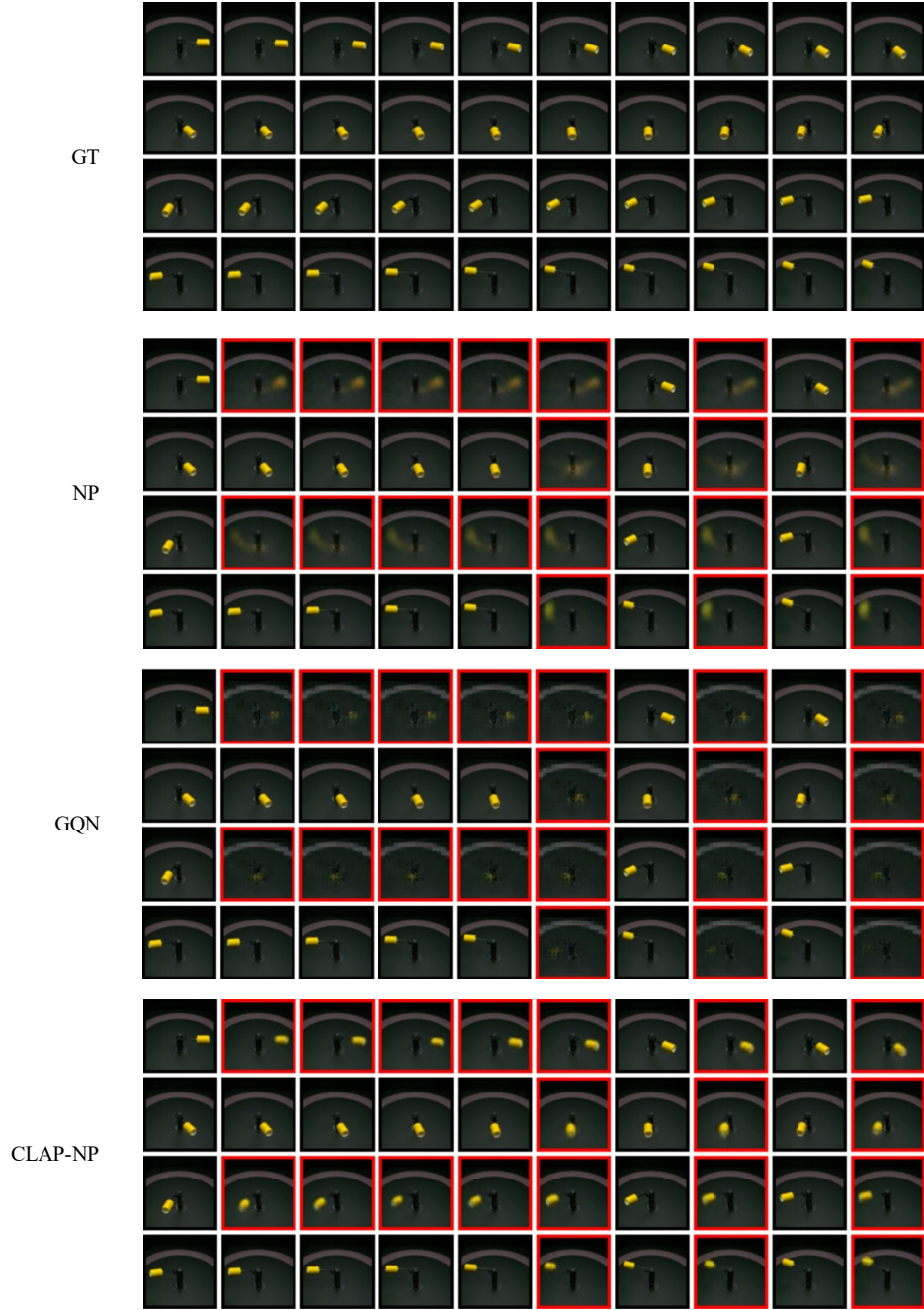
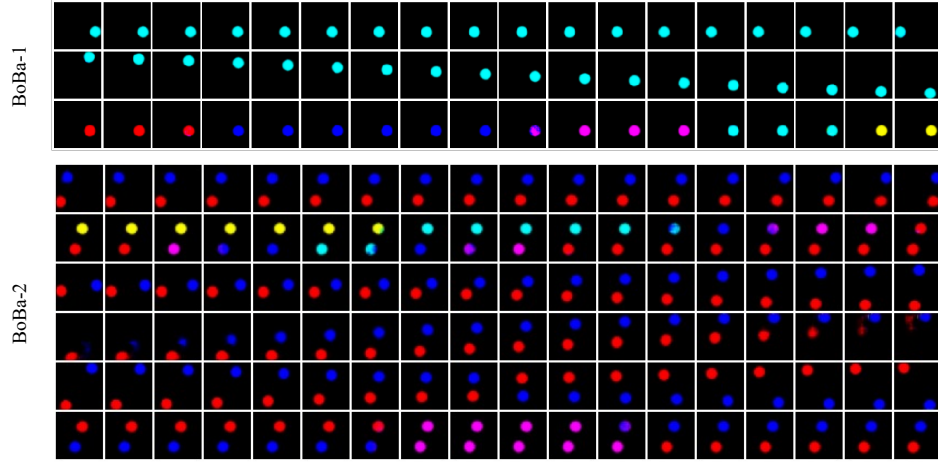
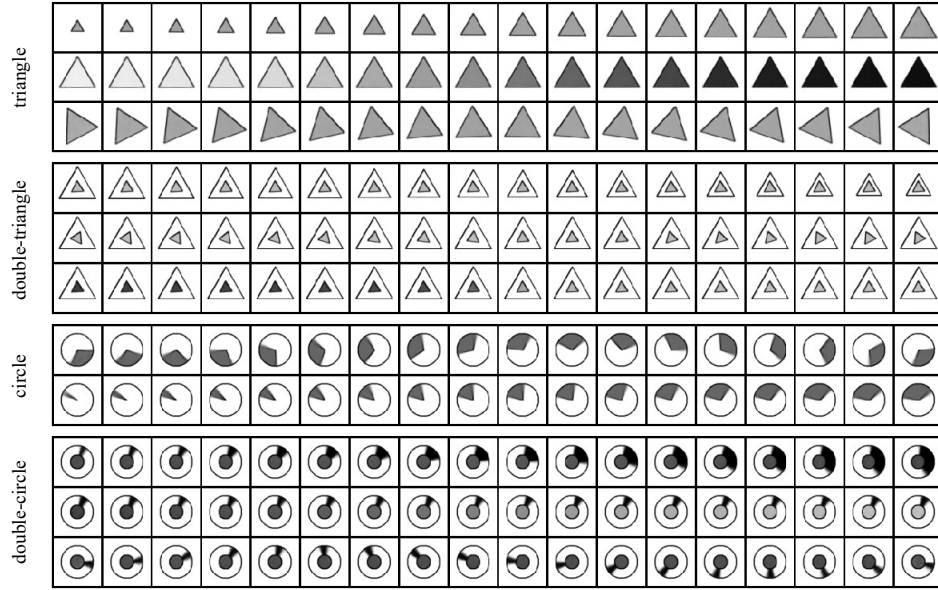


Figure 5: Target prediction with 40 scene images on MPI3D

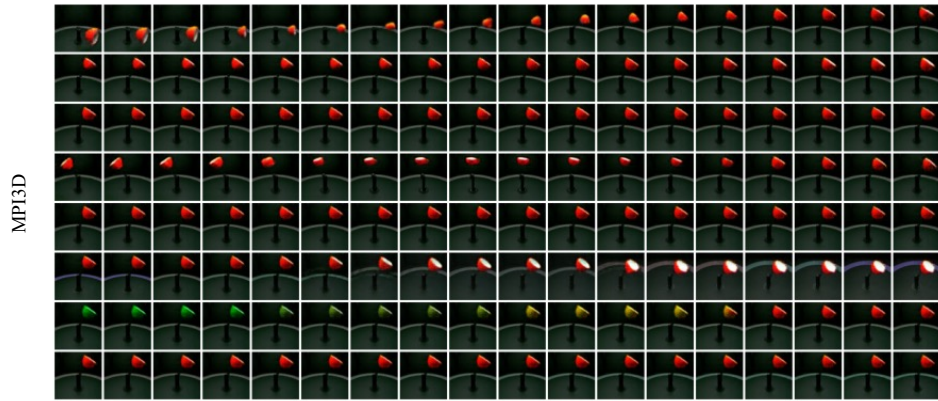




(a) BoBa



(b) CRPM



(c) MPI3D

Figure 6: Concept decomposition of CLAP-NP on three datasets where the concepts are traversed and reconstructed for visualization.

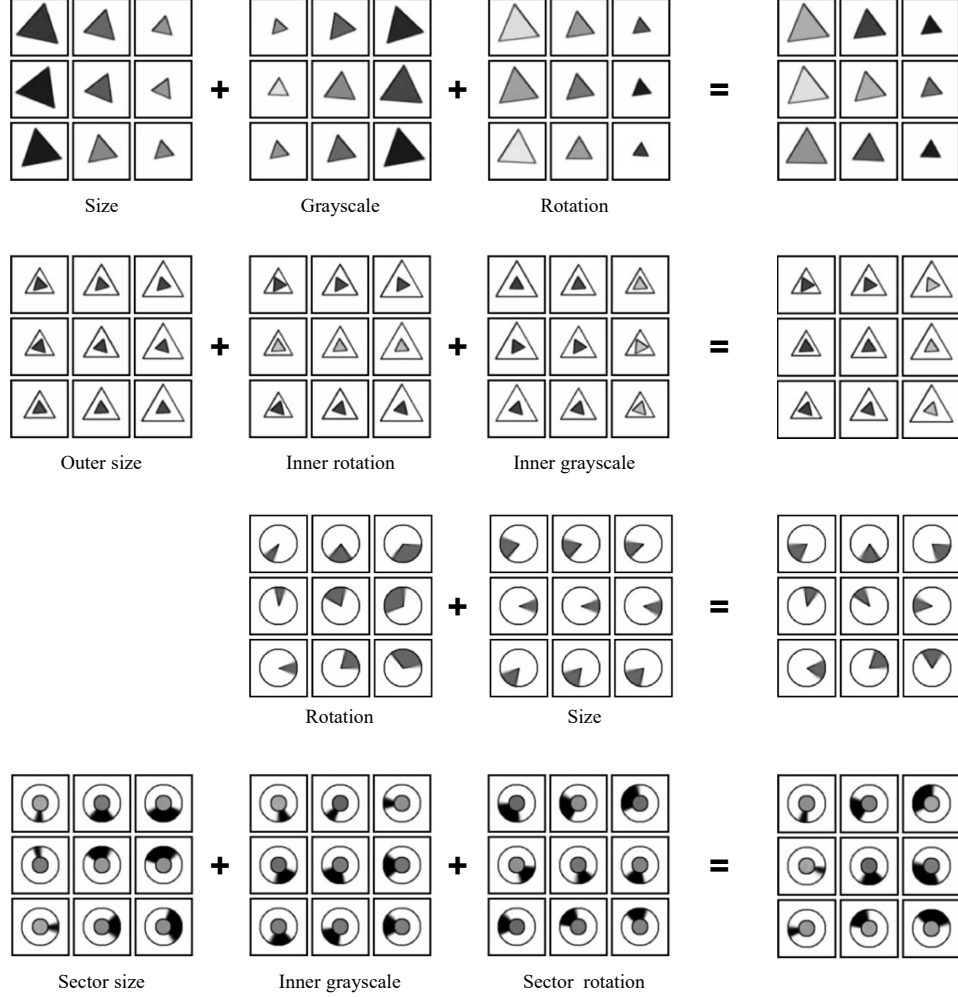
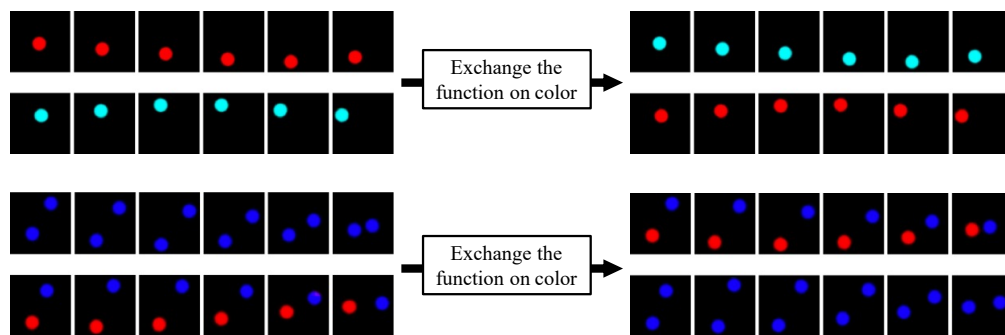


Figure 7: Compose the latent random functions of given samples to generate new samples.

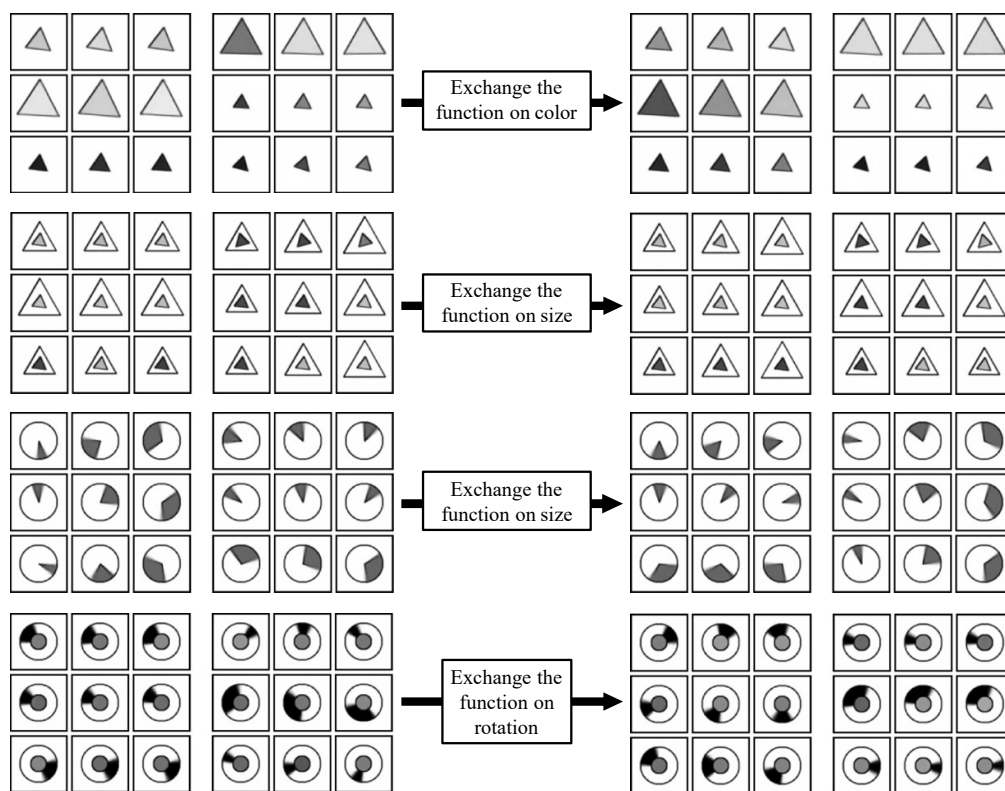
improve the decomposition ability in complex scenes. It is worth noting that images in some of the rows are invariant during the traversal. It indicates the adaptive ability of our model: when we set too many concepts in the configuration, CLAP-NP will use only the necessary number of concepts and automatically ignore the remaining concepts.

**Latent Random Function Composition** By means of concept decomposition, CLAP-NP can parse the latent random function of each concept to represent concept-specific laws, by which the law of a sample can be modified in terms of concepts. Figure 7 displays a way to edit the laws: we compose the concept-specific latent random functions of existing samples to generate samples that have novel changing patterns. For example, in the first sample of Figure 7, we generate a sample with the progressive sizes, progressive grayscales, and constant rotations whose changing patterns come from three given samples. The composition results on four instances of CRPM indicate that CLAP-NP understands the changing patterns on matrices in an interpretable and manipulable way, which embodies the compositionality of human cognition. In this way, we can generate new Raven’s progressive matrices by randomly combining the existent concept-specific rules.

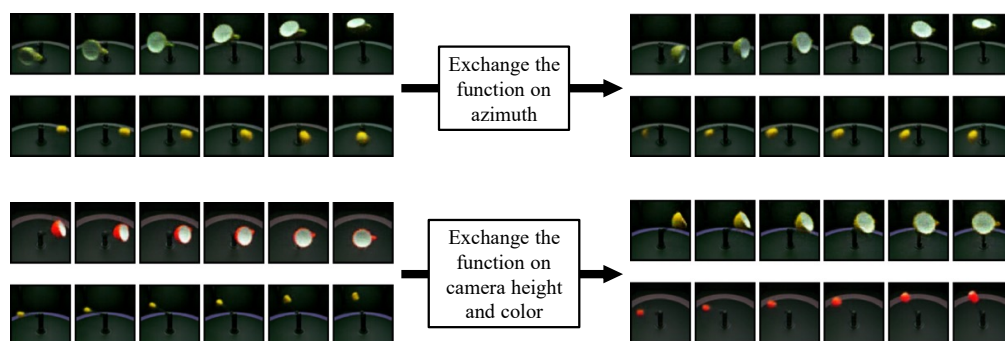
**Latent Random Function Exchange** Another way to edit and manipulate laws is to exchange latent random functions of some concepts between samples. In BoBa, we swap the latent random functions between two samples to change the color of the balls, and the results are shown in Figure 8a. To this end, according to the concept decomposition results in Figure 8a, we exchange the laws on the 3rd concept in BoBa-1 and the rules on the 2nd and 6th concepts in BoBa-2 to realize the color exchange. For CRPM, CLAP-NP displays the ability to generate new samples by exchanging



(a) BoBa



(b) CRPM



(c) MPI3D

Figure 8: Exchange latent random functions of specific concepts.

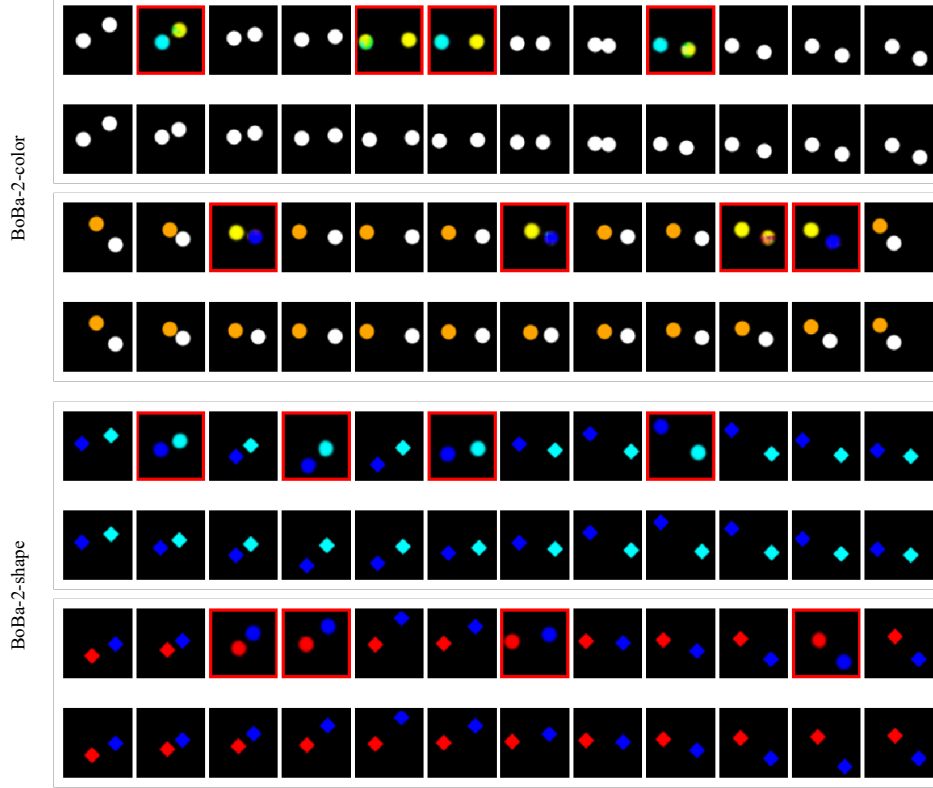


Figure 9: Generalize CLAP-NP to unseen colors and shapes on BoBa-2 dataset.

the latent random function of a concept, which is similar to the latent random function composition experiment described above. In MPI3D, we exchange both variant concepts (azimuth in example 1 of Figure 8c) and invariant concepts (color and camera height in example 2 of Figure 8c). In the first example of Figure 8c, we exchange the latent random functions of the azimuth between samples, where sample 1 and sample 2 respectively change in altitude and azimuth. After the function exchange, sample 1 changes in both the altitude and azimuth, while sample 2 keeps stationary. Both samples are non-existent in the dataset (samples from MPI3D are guaranteed to change in altitude or azimuth), so this experiment well illustrates the ability of CLAP-NP to generate new samples. Overall, the experiment about latent random function exchange evidences the interpretability and manipulability of CALP-NP to modify the laws of data.

**Generalization on Unseen Concepts** We extend BoBa-2 to generate two novel datasets: BoBa-2-color and BoBa-2-shape. Without changing the law of motion, we draw balls in BoBa-2-color with unseen colors and replace the balls in BoBa-2-shape with squares. After training on BoBa-2, CLAP-NP is tested by BoBa-2-color and BoBa-2-shape to evaluate whether the compositionality of laws helps generalization to unseen concepts. The experimental results in Figure 9 show that CLAP-NP correctly predicts the position of objects on both datasets because the compositionality makes the law of motion unrelated to the law of color or shape. However, the color and shape of objects deviate from those of real ones. This phenomenon is intuitive because the encoder and decoder are trained based on BoBa-2, whose latent space does not include unseen colors or shapes. But the correct prediction of trajectory indicates CLAP-NP’s ability to generalize the law of motion to objects with unseen colors and shapes.

**Failure Cases** In this experiment, we display some failure cases. For BoBa, most failure cases occur when there are continuous target images (1st sample of BoBa in Figure 10) or too many target images (2nd sample of BoBa in Figure 10). For CRPM, CLAP can predict target images with diversity when we remove the third row from a matrix, but it sometimes generates target images that break the rules. For example, the color of images keeps invariant in the first two rows, but CLAP generates images in the third row with changing grayscale (samples of CRPM in Figure 10). For MPI3D,

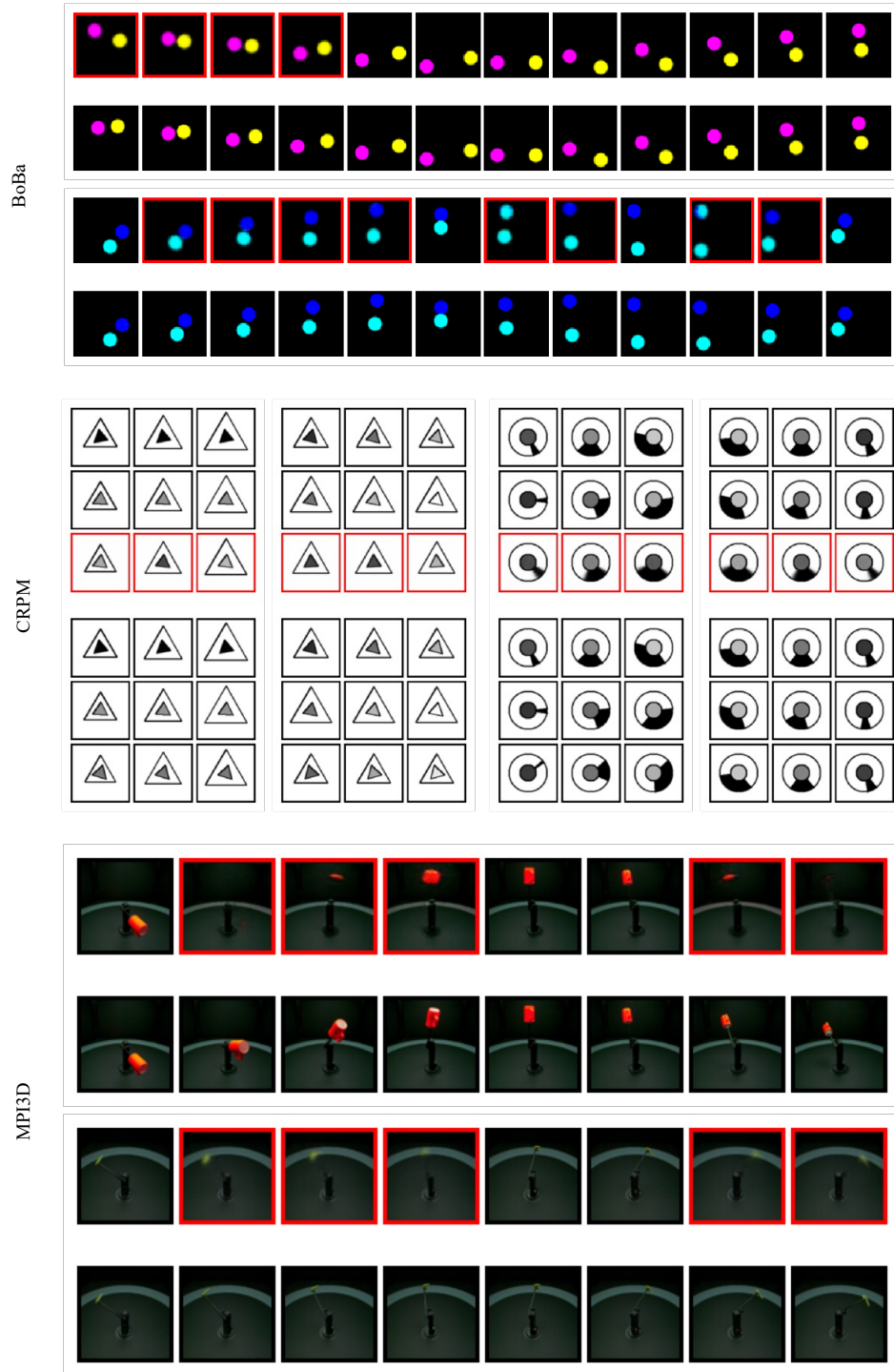


Figure 10: Failure cases on datasets.

when the object size has an obvious change (1st sample of MPI3D in Figure 10) or the centric object is tiny (2nd sample of MPI3D in Figure 10), the predictions will deviate or become unclear.

## References

- [1] Chen, R. T., X. Li, R. B. Grosse, et al. Isolating sources of disentanglement in variational autoencoders. In *Advances in Neural Information Processing Systems*, pages 2610–2620. 2018.
- [2] Gondal, M. W., M. Wuthrich, D. Miladinovic, et al. On the transfer of inductive bias from simulation to the real world: a new disentanglement dataset. *Advances in Neural Information Processing Systems*, 32, 2019.
- [3] Eslami, S. A., D. Jimenez Rezende, F. Besse, et al. Neural scene representation and rendering. *Science*, 360(6394):1204–1210, 2018.
- [4] Kingma, D. P., J. Ba. Adam: A method for stochastic optimization. In *International Conference on Learning Representations*. 2015.
- [5] Garnelo, M., J. Schwarz, D. Rosenbaum, et al. Neural processes. *arXiv preprint arXiv:1807.01622*, 2018.
- [6] Paszke, A., S. Gross, F. Massa, et al. Pytorch: An imperative style, high-performance deep learning library. *Advances in neural information processing systems*, 32, 2019.